



저작자표시-비영리-변경금지 2.0 대한민국

이용자는 아래의 조건을 따르는 경우에 한하여 자유롭게

- 이 저작물을 복제, 배포, 전송, 전시, 공연 및 방송할 수 있습니다.

다음과 같은 조건을 따라야 합니다:



저작자표시. 귀하는 원저작자를 표시하여야 합니다.



비영리. 귀하는 이 저작물을 영리 목적으로 이용할 수 없습니다.



변경금지. 귀하는 이 저작물을 개작, 변형 또는 가공할 수 없습니다.

- 귀하는, 이 저작물의 재이용이나 배포의 경우, 이 저작물에 적용된 이용허락조건을 명확하게 나타내어야 합니다.
- 저작권자로부터 별도의 허가를 받으면 이러한 조건들은 적용되지 않습니다.

저작권법에 따른 이용자의 권리는 위의 내용에 의하여 영향을 받지 않습니다.

이것은 [이용허락규약\(Legal Code\)](#)을 이해하기 쉽게 요약한 것입니다.

[Disclaimer](#)

이학박사 학위논문

Impulsive Wave Excitation in the Solar Atmosphere

태양 대기에서 관측되는 음파의 충동적 발진 연구

2021년 2월

서울대학교 대학원
물리·천문학부 천문학전공
곽한나

Impulsive Wave Excitation in the Solar Atmosphere

태양 대기에서 관측되는 음파의 충동적 발진 연구

지도교수 채 종 철

이 논문을 이학박사 학위논문으로 제출함

2020년 10월

서울대학교 대학원

물리·천문학부 천문학전공

곽 한 나

곽 한 나의 이학박사 학위논문을 인준함

2020년 12월

위 원 장

김 용 터

부 위 원 장

채 종 철

위 원

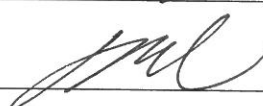
윤 승 철

위 원

최 광 선

위 원

권 윤 영



Impulsive Wave Excitation in the Solar Atmosphere

by

Hannah Kwak

A dissertation submitted in partial fulfillment of the requirements for
the degree of

Doctor of Philosophy

in

Astronomy

in

Astronomy Program

Department of Physics and Astronomy

Seoul National University

Committee:

Professor Woong-Tae Kim

Professor Jongchul Chae

Professor Sung-Chul Yoon

Professor Gwang-Son Choe

Doctor Ryun-Young Kwon

ABSTRACT

Oscillations and waves are commonly observed in the Sun. The understanding of these waves is crucial as they provide information about the medium they pass through. The waves depend on the temperature, density, and structure of the magnetic field in the solar atmosphere, and they are also related to various physical processes occurring in the solar atmosphere. Therefore, waves are very useful diagnostic tools for studying the structures of the solar atmosphere and the various physical processes occurring in there. Moreover, waves transport energy from the interior or surface of the Sun to the upper atmospheric layers. It is believed that waves contribute to the chromospheric and coronal heating. Despite years of research, the origin of the waves is still not well established. The excitation of waves has been well studied from a theoretical point of view, and it requires now intensive observational exploration. In this thesis, we investigate the occurrence of acoustic waves in the solar atmosphere that are generated by impulsive disturbances. For this study, we obtained high-spatial and high-spectral resolution data with the Fast Imaging Solar Spectrograph (FISS) of the 1.6 m Goode Solar Telescope (GST) at the Big Bear Solar Observatory (BBSO) and the Interface Region Imaging Solar Spectrograph (IRIS).

First, we investigated three-minute sunspot oscillations generated impulsively by a strong downflow event above a sunspot. These oscillations were different from the typical three-minute oscillations that are persistently observed in sunspot umbrae. The strong downflow event was identified in the chromospheric and transition region lines above the sunspot umbra. After the event, oscillations occurred at the same region. We also investigated the properties of the Doppler velocity oscillations. The amplitude of the oscillations was 2 km s^{-1} , and gradually decreased with time. In addition, the period of the oscillations gradually increased from 2.7 minutes to

3.3 minutes. In the IRIS 1330 slit-jaw images, we identified a transient brightening near the footpoint of the downflow detected in the $H\alpha+0.5 \text{ \AA}$ image. The characteristics of the downflowing material are consistent with those of sunspot plumes. Based on our findings, we suggest that the gravitationally stratified atmosphere came to oscillate with three minute period in response to the impulsive downflow event as was theoretically investigated by Chae & Goode (2015).

Second, we investigated wave excitations in quiet region that are associated with rapidly changing granules in the photosphere. The observations were carried out with the FISS in the $H\alpha$ and $\text{Ca II } 8542 \text{ \AA}$ lines and the $\text{TiO } 7057 \text{ \AA}$ broadband filter imager of the 1.6 m GST at the BBSO. We identified granules in the internetwork region that undergo rapid dynamic changes such as collapse (event 1), fragmentation (event 2), or submergence (event 3). These granules become significantly darker than the neighboring granules in the photospheric images. After the rapid changes of the granules, transient oscillations were detected in the photospheric and chromospheric layers. In the case of event 1, the dominant period of the oscillations was close to 4.2 min in the photosphere and 3.8 min in the chromosphere. Moreover, in the $\text{Ca II } -0.5 \text{ \AA}$ raster image, we observed repetitive brightenings in the location of the rapidly changing granules that are considered the manifestation of shock waves. Based on our results, we suggest that dynamic changes of granules can generate upward-propagating acoustic waves in the quiet Sun that ultimately develop into shocks.

Third, we studied the occurrence of internetwork bright grains and the associated temperature variations in the upper chromosphere. The bright grains are small-scale intermittent brightenings that are regarded as shocks formed in the chromosphere. From the analysis of high-resolution spectral data taken with FISS in the $H\alpha$ and $\text{Ca II } 8542 \text{ \AA}$ lines, we found four internetwork bright grain events in the Ca II raster images. We investigated the variations of the Ca II line intensity and temperature

above the bright grains and obtained their spatio-temporal relationship. Prior to the appearance of the bright grains in the chromospheric layers, darkening of the intergranular lanes were observed in the photosphere, which are regarded as convective downflows. The strongest event was investigated in detail and a temperature increase of about 7000 K was obtained during the brightenings. The temporal variations of the Ca II line profiles indicate that the bright grains were produced by shocks as the bright grains occur between the maximum redshift and the maximum blueshift. Our results suggest that photospheric waves excited by convective downflows propagate upwards into the chromosphere and cause temperature increase in the upper chromosphere as shocks dissipate.

Overall, our results suggest that the solar acoustic waves are often generated by impulsive events in the solar atmosphere. These waves propagate upward and the energy carried by waves eventually dissipates into heat in the chromosphere.

Keywords: Sun: atmosphere – Sun: photosphere – Sun: chromosphere – Sun: oscillations – Sun: sunspots – methods: observational

Student Number: 2012-20397

Contents

Abstract	i
List of Figures	ix
1 Introduction	1
1.1 Waves in the solar atmosphere	1
1.1.1 Waves in sunspots	2
1.1.2 Waves in quiet region	6
1.2 Importance of the wave study	9
1.3 Purpose of this thesis	13
1.4 Instruments	14
1.5 Outline of this thesis	17
2 Oscillatory Response of the Solar Chromosphere to a Strong Down- flow Event above a Sunspot	19
2.1 Introduction	19
2.2 Observations and data analysis	21
2.3 Results	24
2.4 Discussion	30

3	Impulsive Wave Excitation by Rapidly Changing Granules	33
3.1	Introduction	33
3.2	Observations and data analysis	36
3.3	Results	41
3.3.1	Dynamically changing granules	42
3.3.2	Wave excitation	46
3.3.3	Wave propagation and influence on the higher atmosphere . .	52
3.3.4	Classic acoustic event	55
3.4	Discussion	55
4	Temperature Variations in Internetwork Bright Grains	61
4.1	Introduction	61
4.2	Observations and data analysis	64
4.3	Results	66
4.4	Discussion	78
5	Summary and Conclusion	83
	Bibliography	86
	요 약	93

List of Figures

1.1	A continuum intensity image of sunspots taken with the Helioseismic and Magnetic Imager of the Solar Dynamics Observatory	3
1.2	Images of a sunspot observed in the blue continuum (photosphere; upper left), $H\alpha$ core (chromosphere; upper middle), and the chromospheric power maps	7
1.3	Acoustic power averaged over the period range 150–190 s, overlaid on a continuum image.	10
1.4	An example of internetwork bright grains.	11
1.5	Left: the 1.6 m Goode Solar Telescope (GST). Right: the Fast Imaging Solar Spectrograph (FISS) installed on a vertical table of Coudé room.	15
1.6	IRIS spacecraft in clean room	16
2.1	Images of the small sunspot taken by the FISS, IRIS and SDO at 17:30 UT on 2014 September 27	22
2.2	Wavelength-time plots of the five spectral lines	25
2.3	Temporal variations of the LOS Doppler velocity in different lines	27
2.4	Images of the FISS $H\alpha$ LOS Doppler velocity map, $H\alpha+0.5 \text{ \AA}$, IRIS SJI 1330 \AA and AIA 171 \AA during the strong downflow event	29
3.1	Photospheric TiO 7057 \AA broadband filter image of a quiet Sun region taken at 18:03:56 UT ($t = 11.9 \text{ min}$)	37

3.2	Fourier power spectra and noise models for the $H\alpha$ (upper panel) and $Ti\ II$ (lower panel) data	40
3.3	Temporal evolutions of the granule of event 1 in the TiO images and the $H\alpha-4\ \text{\AA}$ raster images	43
3.4	Temporal evolutions of the granule of event 2 in the TiO images and the $H\alpha-4\ \text{\AA}$ raster images	44
3.5	Temporal evolutions of the granule of event 3 in the TiO images and the $H\alpha-4\ \text{\AA}$ raster images	45
3.6	Time series of the TiO images (first row), $H\alpha-4\ \text{\AA}$ raster images (second row), and vertical velocity maps of the $Ti\ II$ (third row) and $H\alpha$ (fourth row) for event 1	47
3.7	Time series of the TiO images (first row), $H\alpha-4\ \text{\AA}$ raster images (second row), and vertical velocity maps of the $Ti\ II$ (third row) and $H\alpha$ (fourth row) for event 2	48
3.8	Time series of the TiO images (first row), $H\alpha-4\ \text{\AA}$ raster images (second row), and vertical velocity maps of the $Ti\ II$ (third row) and $H\alpha$ (fourth row) for event 3	49
3.9	Temporal variations of the $H\alpha$ and $Ti\ II$ vertical velocities and the TiO intensity (left). Wavelet power spectra (right)	51
3.10	TiO image (top left) and photospheric wave energy flux map (top right) at $t = 15.4\ \text{min}$	53
3.11	TiO image (top left), the $Ca\ II-0.5\ \text{\AA}$ raster image (bottom left) at $t = 15.1\ \text{min}$ and the wavelength-time ($\lambda - t$) plot of the $Ca\ II\ 8542\ \text{\AA}$ line intensity (right)	54
3.12	Time series of the TiO images (first row), $H\alpha-4\ \text{\AA}$ raster images (second row), and vertical velocity maps of the $Ti\ II$ (third row) and $H\alpha$ (fourth row) for a classic acoustic event	56

4.1	Photospheric TiO 7057 Å broadband filter image of a quiet-Sun region taken at 18:03:56 UT	63
4.2	Three-layer model of radiative transfer consisting of two chromospheric layers and one photospheric layer	65
4.3	Time series of the Ca II+0.0 Å raster images (first row), temperature maps (second row), the Ca II-4 Å raster images (third row), and vertical velocity maps of the photosphere (fourth row) for event 1 . . .	67
4.4	Time series of the Ca II-4 Å raster images (first row), the Ca II+0.0 Å raster images (second row), temperature maps (third row), and vertical velocity maps of the photosphere (fourth row) for event 2 . . .	68
4.5	Time series of the Ca II-4 Å raster images (first row), the Ca II+0.0 Å raster images (second row), temperature maps (third row), and vertical velocity maps of the photosphere (fourth row) for event 3 . . .	69
4.6	Time series of the Ca II-0.5 Å raster images (first row), temperature maps (second row), the Ca II-4 Å raster images (third row), and vertical velocity maps of the photosphere (fourth row) for event 4 . . .	70
4.7	Temporal variations of temperature, intensity, vertical velocity and source functions at a fixed position of bright grains in event 1	73
4.8	Temporal variations of temperature, intensity, vertical velocity and source functions at a fixed position of bright grains in event 2	74
4.9	Temporal variations of temperature, intensity, vertical velocity and source functions at a fixed position of bright grains in event 3	75
4.10	Temporal variations of temperature, intensity, vertical velocity and source functions at a fixed position of bright grains in event 4	76
4.11	Wavelength-time plot ($\lambda - t$) of the Ca II 8542 Å line intensity (left), Ca II line profiles (top right), and contrast profiles (bottom right) . .	79
4.12	Temporal variations of the velocities and intensity	80

Chapter 1

Introduction

1.1 Waves in the solar atmosphere

A variety of oscillations and waves have been observed in the Sun. They are identified as periodic fluctuations of intensity and velocity. As a matter of fact, they exist in all layers in the solar atmosphere and even in the solar interior. In the photosphere, oscillations with a wide range of periods are present, but the power is concentrated at the period of 5 min. The 5 min oscillations are detected ubiquitously and persistently in the photosphere. According to numerous studies, they are the indication of global acoustic modes that are trapped below the solar surface called p-modes (e.g., Ulrich 1970; Deubner 1975). The origin of these oscillations is thought to be linked to turbulent convection near the solar surface (Goldreich & Kumar 1990).

In the chromosphere, in contrast, oscillations of 3 min period become predominant. The waves present in the photosphere can propagate upward if their period is shorter than 3 min (5.2 mHz in frequency), the cutoff period. The acoustic cutoff frequency is defined as the ratio of the local sound speed c_s to twice the pressure scale height H_p . Since the pressure scale height is expressed as $H_p = c_s^2/\gamma g$, the

acoustic cutoff frequency is given by the expression

$$\omega_c = \frac{\gamma g}{2c_s}, \quad (1.1)$$

where γ is the specific heat ratio, and g is the gravitational acceleration. In magnetized regions, however, the acoustic cutoff frequency can be lowered and the waves that have longer periods (around 5 min or higher) can propagate upward. It is because the effective gravitational acceleration g_{eff} can be reduced when the waves propagate along inclined magnetic field lines, which is given as $g_{eff} = g \times \cos \theta$. Therefore, in the regions of strong and inclined magnetic field lines, oscillations with periods longer than 3 min can be found in the upper atmosphere.

Oscillations and waves are detected in diverse structures of the Sun such as loops, filaments, sunspots, network, internetwork regions, etc. These different structures are dominated by different periods of oscillations. In particular, in the regions of sunspot umbra and internetwork, the 3 min period chromospheric oscillations are prevail.

1.1.1 Waves in sunspots

Sunspots are dark spots that can be observed on the solar surface in continuum intensity images (Figure 1.1). They look darker than the surroundings because the temperature of the sunspots is lower than those of the neighboring regions. The temperature is lower by 1000 to 1900 K than the surroundings (~ 6000 K). The reason for the lower temperature of the sunspots is that strong magnetic flux concentrations hinder convection and prevent the heat transfer. Typically sunspots consist of a dark umbra and a less darker penumbra that surrounds the umbra. The magnetic field lines are close to vertical in the umbra region, while they are more inclined in the penumbra region.

Observations of oscillations and waves in sunspots have a long history. The existence of waves in sunspots was first revealed by Beckers & Tallant (1969), and since



Figure 1.1 A continuum intensity image of sunspots taken with the Helioseismic and Magnetic Imager of the Solar Dynamics Observatory (<https://sdo.gsfc.nasa.gov/gallery/main/item/146>).

then significant progress has been made by numerous subsequent studies. Now it is clearly demonstrated that waves in sunspot umbra and penumbra have different characteristics, and waves in different atmospheric layers show different properties. Generally, they are observed as periodic fluctuations of the intensity and velocity.

In umbra regions, velocity oscillations observed in the photospheric layers are similar to those of the surrounding quiet region. The dominant period of umbral oscillations is around 5 min, which is analogous to that of the quiet region oscillations in the photosphere. However, the amplitude of the oscillations is highly reduced in the umbra region compared to the quiet region oscillations (Howard et al. 1968). In photospheric velocity power spectra, most of the power is concentrated in the 5 min band, but it also has a secondary peak in the 3 min band (Lites & Thomas 1985; Centeno et al. 2006). Nevertheless, Lites (1986) reported that the regions of a high 3 min power are not correlated with those of high 5 min power regions.

In the chromosphere, the 3 min period velocity oscillations become predominant. It is widely accepted that the 3 min power of the chromospheric oscillations comes directly from the photosphere (Centeno et al. 2006; Kobanov et al. 2013). The 3 min umbral oscillations are nonlinear in the chromosphere and they are regarded as shock waves since the sawtooth pattern is clearly identified in the Doppler shift oscillations of various chromospheric lines (e.g., Rouppe van der Voort et al. 2003; Tian et al. 2014). Moreover, umbral oscillations can reach the upper atmosphere. O'Shea et al. (2002) found the presence of velocity oscillations in various atmospheric layers from the temperature minimum to the upper corona above an umbral region. The properties of the oscillations found in the transition region and corona is similar to those of the chromosphere. The phase difference measurements between the oscillations obtained from different heights indicate the upward propagation of acoustic waves from the chromosphere to the transition region (Brynildsen et al. 1999). Meanwhile, the 3 min umbral oscillations are also called umbral flashes as

observed as brightness fluctuations in the Ca II H and K lines (Beckers & Tallant 1969). The period of the umbral flashes is about 2–3 min and velocity oscillations are observed simultaneously (Beckers & Schultz 1972). Umbral flashes are produced by upward propagating shock waves (Roupe van der Voort et al. 2003).

In penumbra regions, the photospheric velocity oscillations look similar to the umbral oscillations, showing a maximum power in the 5 min band and a weak power in the 3 min band. Nagashima et al. (2007) reported that penumbral oscillations also appear as intensity fluctuations and the power of the penumbral oscillations are suppressed compared to that of the quiet region oscillations. In the chromosphere, waves that propagate radially outward from the inner to the outer penumbra boundary are detected in the H α line core images and these waves are named running penumbral waves (Zirin & Stein 1972; Giovanelli 1972). The dominant period of the running penumbral waves increases as the distance from the inner penumbra increases. Figure 1.2 shows chromospheric power maps at different periodicities. The periods of 300 s oscillations (lower left panel) are predominant at the inner penumbra and the periods of 540 s oscillations (lower right panel) are predominant at the outer penumbra. This period increase along the radial direction is attributed to the magnetic field inclination angles increasing with the radial distance from the inner penumbra as they lower the cutoff frequency in the penumbra region (Jess et al. 2013).

Considering all the characteristics, the oscillations observed in sunspots are attributed to slow magnetoacoustic waves that propagate upward in a gravitationally stratified medium (Centeno et al. 2006; Jess et al. 2013). As mentioned above, the upward propagation of the waves is revealed by investigating the amplitudes and phase differences of the velocity oscillations acquired at different heights (O’Shea et al. 2002; Brynildsen et al. 1999, 2004). Moreover, their upward propagation is guided by the magnetic field lines and it indicates slow mode acoustic waves. The oscillations are observed as fluctuation of intensity and velocity and it is the manifestation

of compressional waves.

For the origin of the waves in sunspots, two major candidates have been proposed. The first one is an external p-mode absorption. Since the properties and the behavior of the oscillations found in the photosphere of sunspots is analogous to those of the quiet Sun (Zhao & Chou 2013), it is reasonable to suggest that the waves may come from p-modes outside the sunspots. The other one is the magnetoconvection in sunspots. The convection is highly suppressed in sunspots due to the strong magnetic field, but it is possible in some field-free regions such as umbral dots and light bridges. According to recent studies, chromospheric 3 min oscillations are identified above umbral dots (Cho et al. 2019) and light bridges (Chae et al. 2017), which are considered as the result of small-scale magnetoconvection in sunspots.

1.1.2 Waves in quiet region

The solar quiet region is the region outside active regions such as sunspots, plages, and coronal holes. A quiet region can be divided into two subregions, network and internetwork regions. The formation of the network and internetwork regions is associated with the supergranulation, which is the convective flow at scales of 30 Mm. In the center of the supergranulation cells, upward motions and diverging horizontal flows are prevalent. On the contrary, at the boundaries of the supergranulation cells, downward motions and converging flows are dominant. As a result, small-scale magnetic flux concentrations gather at the boundaries of the supergranulation cells and form the network regions, while the supergranulation interior forms the internetwork region. The network region is well revealed by bright web-like structures in the Ca II H chromospheric images. In the network region, low frequency oscillations with periods of 5–20 min are predominant in the chromospheric layer (Lites et al. 1993; Vecchio et al. 2007). These low frequency waves are thought to originate from photospheric p-modes, as the inclined magnetic fields lower the acoustic cutoff

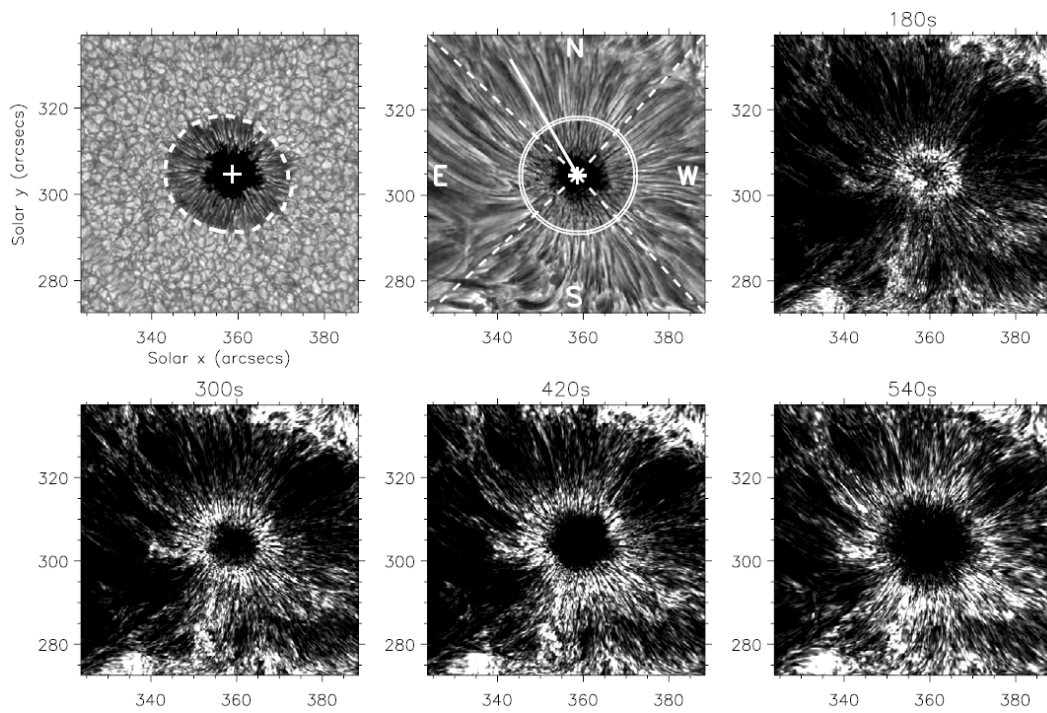


Figure 1.2 Images of a sunspot observed in the blue continuum (photosphere; upper left) and H α core (chromosphere; upper middle). The remaining panels show the chromospheric power maps obtained from Fourier analysis of the H α time series. In each power map, white colored region indicates the location of high power with periods of 180, 300, 420, and 540 s (Jess et al. 2013).

frequency (Jefferies et al. 2006; Vecchio et al. 2007). The understanding of the oscillations and waves in this magnetized region is challenging because of the interaction of the waves with the magnetic field.

In the internetwork region, oscillations with 3 min periods are commonly observed in the chromosphere (Orrall 1966). From multi-wavelength observations, Kayshap et al. (2018) investigated Doppler velocity oscillations in the photosphere (Mn I 2801.25 Å), chromosphere (Mg II 2796.35 Å), and transition region (C II 1334.53 Å). In the photosphere, oscillations with a period range from 2 to 6 min are found. In the chromosphere, the power of the velocity oscillations are concentrated in the period range of 2–4 min. Similarly, in the transition region, oscillations with a period range from 2 to 4 min are dominant. The wave propagation is also examined in the internetwork region from the photosphere to the transition region. In the short period regime, i.e., a period range from 1.6 to 4 min, waves successfully propagate upward from the photosphere to the chromosphere. In addition, waves with a period of 2.5 to 6 min propagate upward from the chromosphere to the transition region. In contrast, the oscillations with periods longer than 4.5 min propagate downward from the chromosphere to the photosphere, and it is thought to be the effect of the cutoff frequency.

The most intensely studied wave phenomena in the internetwork region are the acoustic events and internetwork bright grains. Both type of events are related to the 3 min oscillations in the internetwork region. The acoustic events are defined as a spatially localized transient wave energy flux, and are the result from the excitation of waves beneath the photosphere (Rimmele et al. 1995). The acoustic events are mainly identified in intergranular lanes, the space between the granules (Rimmele et al. 1995; Bello González et al. 2010). Figure 1.3 shows that most of the power is concentrated in the intergranular lanes. The intergranular lanes are well-known as the regions with strong downflows, because the material raised by the convective

flows rapidly descends in this region. Theoretical studies in accordance with the observational investigations, suggest that the acoustic events are generated by localized cooling that is accompanied by strong downflows or by the collapse of small granules (Rast 1999; Skartlien et al. 2000).

The internetwork bright grains are small-scale ($1''$ – $2''$) brightenings observed in the internetwork region of the chromosphere. In particular, they are prominent in the Ca II H and K filtergrams and time series of spectra (e.g., Bappu & Sivaraman 1971; Zirin 1974; Cram & Dame 1983). The bright grains are transient (~ 1 min) and occur intermittently at 3 min intervals (see the extensive review by Rutten & Uitenbroek 1991). Because of their recurrent nature, they are considered to originate from waves. Carlsson & Stein (1997) carried out one-dimensional non-local thermodynamic equilibrium radiation-hydrodynamic simulations, and reproduced the generation and the behavior of the bright grains by driving acoustic waves in the photosphere. They suggested that the bright grains are generated by waves from the photosphere that eventually develop into shocks in the mid-chromosphere. In addition, the observational study of Kamio & Kurokawa (2006) showed that the internetwork bright grains are produced by shocks in the chromosphere that are associated with the 5 mHz (i.e., 3 min period) oscillations in the photosphere. Interestingly, it is suggested that the internetwork bright grains spatially coincide with the acoustic events, which have the largest acoustic flux in the photosphere (Hoekzema et al. 2002).

1.2 Importance of the wave study

Oscillations and waves are ubiquitous in the solar atmosphere. However, our knowledge about their origin still remains limited. Waves can provide clues about their excitation sources. They are produced by disturbances in a medium, and therefore the excitation of waves implies the occurrence of events that cause these disturbances.

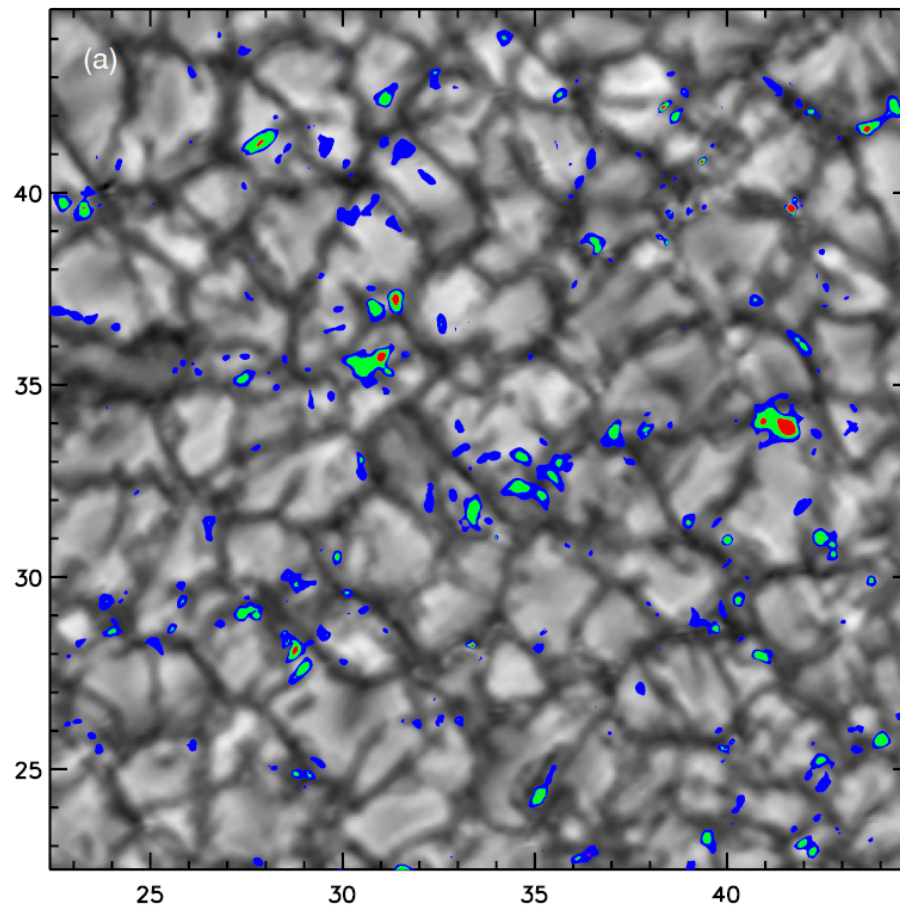


Figure 1.3 Acoustic power averaged over the period range 150–190 s, overlaid on a continuum image. The filled contours indicate 12% (blue), 20% (green) and 32% (red) of the maximum power value over the sequence (Bello González et al. 2010).

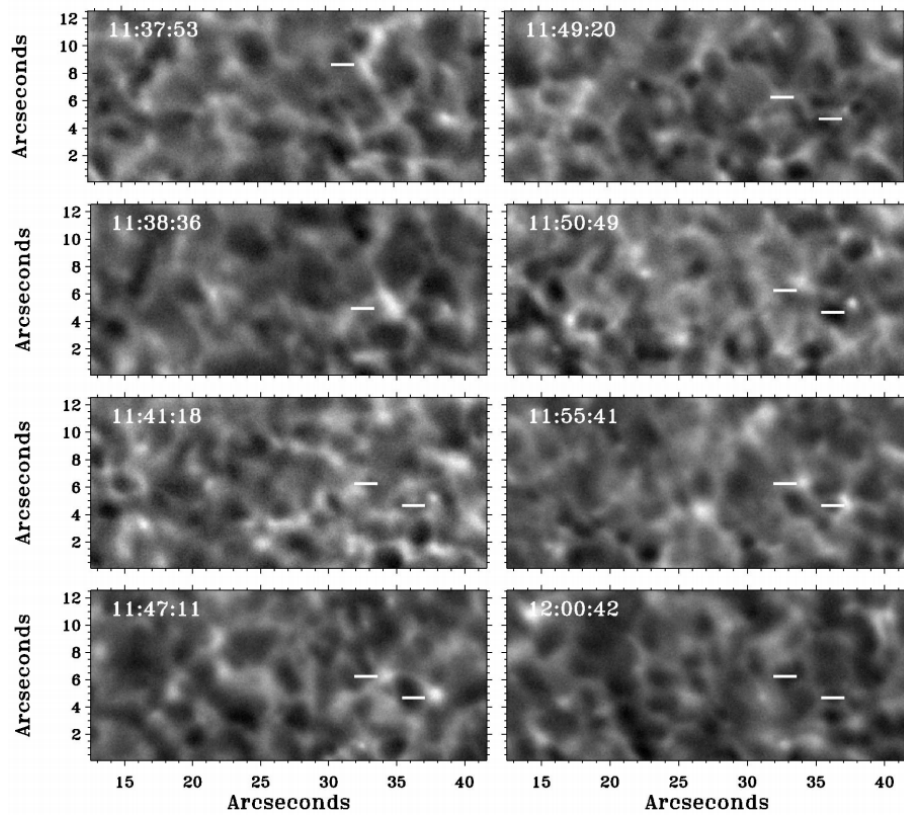


Figure 1.4 An example of internetwork bright grains from the La Palma Ca II K time sequence. The two markers in the panels from 11:41:18 UT to 12:00:42 UT indicate two concurrent K_{2V} grains that are recurrent at 2–3 min intervals (Lites et al. 1999).

The excited waves propagate out of the disturbed region. Since the waves generally keep their properties while propagating outward, the wave excitation sources can be revealed by investigating these propagating waves. Furthermore, in this way, we can identify the probable locations and conditions where waves are likely to occur.

The oscillations and waves in the solar atmosphere also provide information about the medium they pass through. As the Earth's seismic waves have been used for investigating subsurface structures of the Earth, waves in the Sun can be used to get information about the solar interior and the physical properties of the plasmas constituting the solar atmosphere. In the case of the solar interior, this approach has been successfully employed. From the global oscillations trapped inside the solar surface, various properties of the solar interior are determined such as the depth of the convective zone, its temperature profile and the internal rotational speeds. Similarly, in the solar atmosphere, it is expected that oscillations and waves reflect the properties of the medium such as the temperature, density, and magnetic field structures. Therefore, the waves in the solar atmosphere can be a useful tool for studying the structures of the solar atmosphere and a variety of physical processes within it.

Moreover, waves play an important role in transporting energy from the photosphere to the corona. The waves generated near the photosphere or below propagate into the upper atmosphere. Since the density decreases exponentially with height, the waves propagating upward encounter lower and lower density. Thus, the amplitude of the waves increases with height and the waves ultimately develop into shock waves. The energy carried by the waves is then dissipated in the upper atmosphere in the form of heat. It is believed that waves significantly contribute to the chromospheric and coronal heating.

Thanks to the successful development of state-of-the-art instruments and observational techniques, high quality data with ever improving spatial and temporal

resolution are provided. Therefore, the wave studies have the potential to endeavour new research topics and new wave phenomena could be identified. For instance, much shorter period of oscillations can be detected as well as oscillations generated by small-scale activities, which can improve our understanding on their impact on the physical properties of the solar atmosphere.

1.3 Purpose of this thesis

Even though oscillations and waves are commonly observed in the solar atmosphere, we still do not fully understand their origin. In the case of global p-modes, it is now widely accepted that their excitation is attributed to turbulent convection that occurs ubiquitously at the top of the convection zone (Goldreich & Kumar 1990). Similarly, in the solar atmosphere, it is expected that local disturbances generated by impulsive events can lead to acoustic waves (e.g., Chae & Goode 2015). Early theoretical studies suggest that acoustic waves with an acoustic cutoff frequency can be excited by impulsive disturbances in the solar atmosphere (Lamb 1909; Kalkofen et al. 1994). In particular, Chae & Goode (2015) reported that acoustic waves can naturally arise by the occurrence of impulsive disturbances of large vertical extent in a gravitationally stratified medium.

The purpose of this thesis is to improve our knowledge of the generation of waves in the solar atmosphere. Since waves are expected to be caused by impulsive events, we investigate individual wave excitation events in a sunspot umbra and quiet-Sun regions. In addition, we investigate the properties of waves generated by impulsive events and their propagation into the upper atmosphere.

1.4 Instruments

The Goode Solar Telescope (GST, Figure 1.5) is installed at Big Bear Solar Observatory (BBSO), California, United States. Ever since its first light observation in 2009, the GST significantly enhanced our knowledge of the Sun by providing high quality data with various instruments installed on it. The GST is an off-axis Gregorian telescope with a clear aperture of 1.6 m. The adaptive optics system consisting of 308 sub-apertures provides diffraction limited images with a spatial resolution of $0''.06$ at 500 nm (Shumko et al. 2014). Currently, five instruments can be used for solar observations. Most of instruments are installed on a vertical optical table of a Coudé room, which is a separate place for the post-focus instruments.

The Fast Imaging Solar Spectrograph (FISS; Chae et al. 2013) is one of the instruments that is installed on the 1.6 m GST (Figure 1.5). The instrument was developed in cooperation with the solar astronomy group of the Seoul National University and the Korea Astronomy and Space Science Institute. The FISS is a dual-band Échelle spectrograph and records the $H\alpha$ and Ca II 8542 Å bands simultaneously. By the fast scanning of a slit over the field-of-view (FOV), the FISS acquires images as well as spectrograms. It provides high quality imaging and spectral data with a spatial pixel size of $0''.16$ and a spectral pixel size of 0.019 Å in the $H\alpha$ band and 0.026 Å in the Ca II band. The time cadence of the FISS depends on the size of the scanning region but generally lies in the range of 20–30 s. This instrument is suitable for studies of waves and dynamic transient phenomena in the chromosphere.

The Interface Region Imaging Spectrograph (IRIS; De Pontieu et al. 2014) is a space-based instrument that was launched in 2013 (Figure 1.6). As the name of the instrument suggests, the IRIS was designed to investigate the chromosphere and the transition region that forms interface region between the photosphere and corona. The IRIS provides spectra and slit-jaw images (SJI) with high-spatial, high-spectral and high-temporal resolutions. The spectra are acquired in one near-ultraviolet

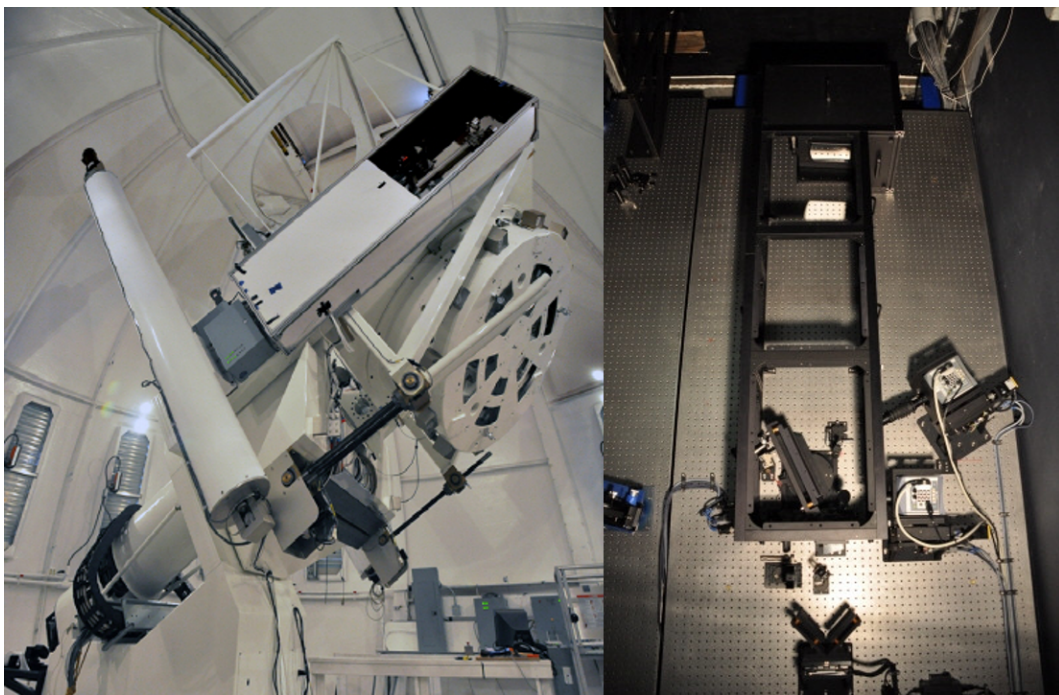


Figure 1.5 Left: the 1.6 m Goode Solar Telescope (GST). Right: the Fast Imaging Solar Spectrograph (FISS) installed on a vertical table of Coudé room.

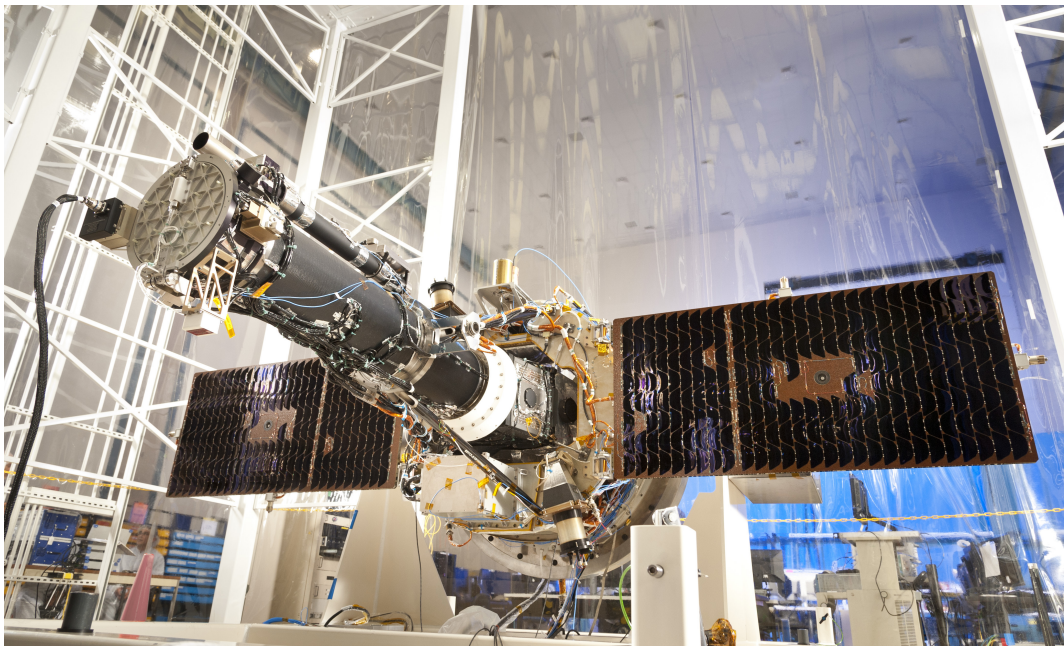


Figure 1.6 Interface Region Imaging Spectrograph (IRIS) spacecraft in clean room with the solar arrays deployed (<https://iris.gsfc.nasa.gov/gallery.html>)

(NUV; 2783–2834 Å) band and two far-ultraviolet (FUV; 1332–1358 Å, 1389–1407 Å) bands. Each spectrum contains strong emission lines that are formed in the chromosphere (Mg II h 2803 Å and Mg II k 2796 Å), in the upper chromosphere and lower transition region (C II 1334/1335 Å), and in the transition region (Si IV 1394/1403 Å). SJI s are obtained with Mg II wing 2830 Å (photosphere), Mg II k 2796 Å (chromosphere), C II 1330 Å (lower transition region) and Si IV 1400 Å (middle transition region) filters. The spatial pixel size is $0''.167$ in both, the spectra and the SJI s. The spectral pixel size is 25.6 mÅ in the NUV passband and 12.8 mÅ in the FUV passbands. The time cadence can differ by settings of the observation mode. Calibrated IRIS level 2 data are provided by IRIS team that are dark current-subtracted, flat-fielded, geometric-corrected, and wavelength-calibrated (De Pontieu et al. 2014). Since the IRIS is a space-based instrument, stable observations are guaranteed and huge amount of data already have been acquired since 2013. Particularly, it is possible to request coordinated observations with ground-based telescopes. From the coordinated observations with FISS, we can trace simultaneously dynamic phenomena and propagating waves in multiple solar atmospheric layers.

1.5 Outline of this thesis

In this thesis, we study the generation of waves in the solar atmosphere by impulsive disturbances. We investigate individual wave excitation events in a sunspot and quiet-Sun regions. The waves produced in the lower atmosphere propagate upward and affect the upper atmosphere by transferring energy. This thesis is structured as follows. In Chapter 2, we report on the occurrence of the chromospheric 3 min oscillations above a sunspot which are driven by a strong downflow event. We investigate the properties of the generated oscillations and compare with theoretical results. In Chapter 3, we present three wave excitation events that are closely related to rapid dynamic changes of granules such as collapse, fragmentation, or submergence. We

calculate the wave energy flux that is produced by the dynamic changes of granules. In Chapter 4, we examine the temperature variations in chromospheric bright grains that are considered to be the observational signature of shocks formed in the mid-chromosphere. The waves that develop into shocks are generated in the photosphere above the intergranular lanes. The summary and conclusions of this thesis are provided in Chapter 5.

Chapter 2

Oscillatory Response of the Solar Chromosphere to a Strong Downflow Event above a Sunspot¹

2.1 Introduction

Ever since discovery of three-minute umbral oscillations (Beckers & Tallant 1969; Beckers & Schultz 1972; Giovanelli 1972), they have been studied for several decades by numerous authors (for reviews, see Staude 1999; Bogdan & Judge 2006; Khomenko & Collados 2015). The oscillations are detected in the multiple layers of the solar atmosphere above sunspot umbrae (e.g., Lites & Thomas 1985; Thomas et al. 1987; Maltby et al. 1999; O’Shea et al. 2002). They are generally manifested as periodic

¹Most of the contents in this chapter were written as a separate paper: Hannah Kwak, Jongchul Chae, Donguk Song, Yeon-Han Kim, Eun-Kyung Lim, Maria S. Madjarska, “Oscillatory Response of the Solar Chromosphere to a Strong Downflow Event above a Sunspot”, 2016, ApJ

fluctuations of intensity and velocity. The oscillations are commonly regarded as slow magnetoacoustic waves upwardly propagating in the gravitationally stratified medium, as the oscillations in the higher atmosphere lag behind those in the lower atmosphere (Brynildsen et al. 1999, 2004; Tian et al. 2014). It is believed that the power of the three-minute oscillations may mostly come from the photosphere or below it. Two specific processes are currently considered as the major candidates for the driver of the oscillations: p -mode absorption of global solar oscillations and magnetoconvection inside sunspots (see review by Khomenko & Collados 2015, and references therein).

Theory predicts that the three-minute umbral oscillations can be excited by impulsive disturbances inside the atmosphere as well. Early studies by Lamb (1909) and Kalkofen et al. (1994) showed that the atmosphere disturbed by an impulsive disturbance at a point begins to oscillate with frequency asymptotically approaching the acoustic cutoff frequency. The recent study of Chae & Goode (2015) found that the necessary condition for the cutoff frequency oscillations to have enough power is the occurrence of the impulsive disturbance of large vertical extent. Since there are many activities in the chromosphere, we expect that impulsive disturbances that produce the three-minute oscillations occur even though they may not be the major driver of such oscillations. Despite this expectation, so far there has been no observational report of such three-minute oscillations generated by impulsive events in the chromosphere above sunspots. This is in contrast with the common findings of oscillations and waves in the corona driven by the strongest impulsive events such as flares (Aschwanden et al. 1999; Nakariakov et al. 1999; Schrijver et al. 2002), lower coronal eruptions/ejections (Zimovets & Nakariakov 2015), and filament destabilizations (Schrijver et al. 2002). Strong X-class flares even affect the solar interior and cause sunquakes which are acoustic waves produced in the photosphere (Kosovichev & Zharkova 1998; Kosovichev 2006). Probably the impulsive events

leading to three-minute oscillations in the chromosphere may be too small and too weak to be detected.

In this chapter, for the first time we report on the occurrence of the three-minute oscillations driven by an impulsive disturbance in the chromosphere. In this specific study, the disturbance was caused by a strong downflow event detected in the chromospheric and transition region (TR) lines above a sunspot umbra. It is important to understand the properties of the oscillations and waves in order to estimate physical quantities of the medium for further study. We analyze multi-wavelength data acquired by the Fast Imaging Solar Spectrograph (FISS; Chae et al. 2013) installed at the 1.6 m New Solar Telescope (NST) of Big Bear Solar Observatory and Interface Region Imaging Spectrograph (IRIS; De Pontieu et al. 2014).

2.2 Observations and data analysis

We observed a small sunspot in NOAA active region 12172 on 2014 September 27. It was located between a leading main sunspot and a trailing main sunspot. The region of our interest was so variable that the morphology of the small sunspot kept changing within several hours, and the sunspot finally disappeared the day after our observation period. The FISS is a dual-band Ech elle spectrograph that records the H α band and the Ca II 8542 Å band simultaneously with imaging capability. Imaging is done by fast scanning of a slit over the field of view (FOV) and the step size is 0."16. With this instrument we acquired data for an hour from 17:03:40 to 18:00:50 UT with the aid of the adaptive optics system. The spatial sampling along the slit is 0."16 and the spectral samplings are 0.019 Å and 0.026 Å at the H α line and the Ca II line, respectively. The FOV of the raster image is 24" \times 40" and the time cadence is 22 s.

The IRIS observation was done with large coarse 2-step raster mode from 11:29:36 to 17:36:50 UT and we analyzed the data taken from 17:03:45 to 17:36:29 UT which

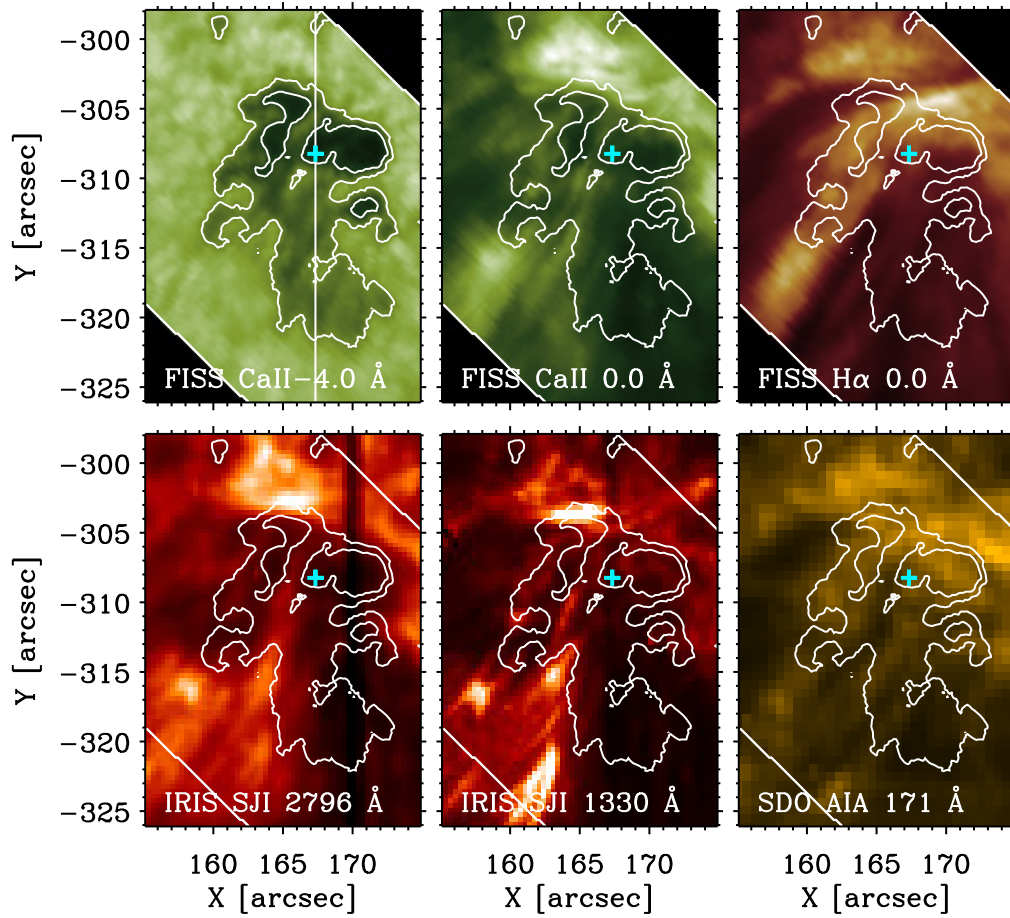


Figure 2.1 Images of the small sunspot taken by the FISS, IRIS and the SDO at 17:30 UT on 2014 September 27. The white vertical line in the FISS Ca II-4 Å image indicates the location of the IRIS slit position, and the cyan cross symbols mark the selected position for detailed analysis in Figure 2.2 and Figure 2.3.

correspond to the overlapping period with the FISS data. The IRIS spectra were acquired in the near-ultraviolet (NUV, 2783–2834 Å) and far-ultraviolet (FUV, 1332–1358 Å, 1390–1406 Å) band, and we utilized Mg II k 2796 Å (formed in the chromosphere), C II 1336 Å (formed in the lower TR) and Si IV 1403 Å (formed in the middle TR) lines for our study. In addition, the IRIS slit-jaw images (SJIs) were taken with the filters of SJI 2796 Å and SJI 1330 Å. The spatial pixel size is 0."33 and the time cadence is 18 s at both of the spectral data and SJIs. We used the IRIS level 2 data which are dark current subtracted, flat-fielded, geometric corrected and wavelength calibrated. Additionally, we used data from the Atmospheric Imaging Assembly (AIA; Lemen et al. 2012) on board the *Solar Dynamics Observatory* (*SDO*) to investigate higher atmospheric responses.

Figure 2.1 shows the small sunspot at different solar atmospheric layers from the upper photosphere to the corona. The FISS Ca II and H α raster images show the low atmosphere from the upper photosphere (line wings) to the chromosphere (line core). The IRIS SJI 2796 Å and SJI 1330 Å correspond to the chromosphere and the lower TR, respectively, and the AIA 171 Å corresponds to the upper TR and the corona. Alignment of the FISS and the IRIS data was carried out by using the FISS Ca II 8542 Å raster image (Figure 2.1 top center panel) and the IRIS SJI 2796 Å image (Figure 2.1 bottom left panel).

We inferred the line-of-sight (LOS) Doppler velocity by applying single Gaussian fit and the lambdameter method to the line profiles. Generally, Mg II and C II line profiles are central-reversed (double-peaked), but inside the sunspot, they are single-peaked and fitted well by the single Gaussian fits (Tian et al. 2014). Similarly, since the Ca II absorption line profiles in sunspot umbrae have an emission core, the core of the line profile is appropriate for applying the single Gaussian fit. Thus, we applied the single Gaussian fits to the line profiles of the Ca II, Mg II, C II and Si IV lines. Whereas, in the case of the H α absorption line profile, we applied the lambdameter

method, which calculates the Doppler velocity by determining the mid-point of $2\Delta\lambda$ (Deubner et al. 1996). We set the $\Delta\lambda$ as 0.5 \AA in this study.

Since the $\text{H}\alpha$ line has a broad absorption core, spectral and temporal variations are not conspicuous in the $\text{H}\alpha$ line profile. Therefore, in order to see the variations clearly, we defined a contrast profile as $C_\lambda = (I_\lambda - I_{ref})/I_{ref}$, where I_λ is the spectral intensity profile at the selected position, and I_{ref} is the reference profile which is a temporally-averaged intensity profile at the same position during our observation period. Using the contrast profiles of the $\text{H}\alpha$ and $\text{Ca II } 8542 \text{ \AA}$ lines, wavelength-time ($\lambda-t$) plots of the intensity contrast are made in Figure 2.2 (f)-(g).

2.3 Results

The remarkable finding of our study is the detection of a strong downflow event and the associated oscillations on the same region. Figure 2.2 shows the $\lambda-t$ plots at a selected position which is marked with a cyan cross symbol in Figure 2.1. The $\lambda-t$ plots represent the spectral and temporal variations in the Ca II , $\text{H}\alpha$, Mg II , C II and Si IV lines. In the plots of the C II and Si IV lines, a striking red-shifted feature suddenly appeared at $t \approx 14$ mins. The red-shifted feature is also identified in the $\lambda-t$ plots of the $\text{H}\alpha$ line, and it stands out more clearly in the $\lambda-t$ plot of the $\text{H}\alpha$ intensity contrast (see Figure 2.2 (g)). We can see that the red-shifted feature showed up first in the $\text{H}\alpha$ line and then in the other lines. In the $\lambda-t$ plot of the $\text{H}\alpha$ intensity contrast, the feature began to appear at $t \approx 10$ mins, and the red shift gradually increased. Four minutes later, in the C II and Si IV lines, the red-shifted feature abruptly showed up and the red shift rapidly increased. This red-shifted feature eventually represents a downflow event occurring in the solar chromosphere and TR.

Interestingly, after the abrupt appearance of the red-shifted feature, oscillation patterns were identified in all of the $\lambda-t$ plots. The red-shifted feature disappeared

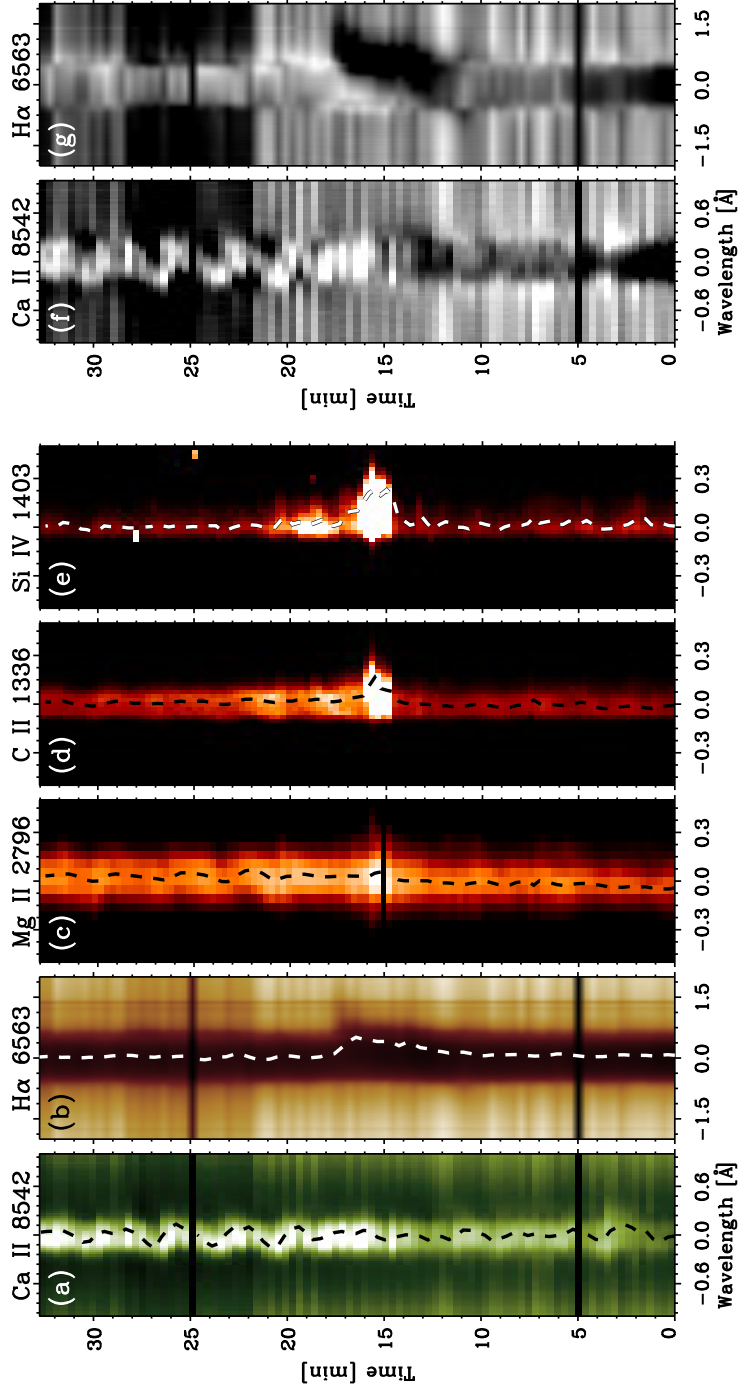


Figure 2.2 Panels (a)-(e) : Wavelength-time ($\lambda-t$) plots of the five spectral lines at the position marked with cyan cross symbols in Figure 2.1. The dashed lines represent the track of the line center obtained by applying the single Gaussian fits to each line (magnified by a factor of 3). Panels (f)-(g) : $\lambda-t$ plots of the Ca II and H α intensity contrast. Time $t = 0$ corresponds to 17:03:40 UT.

at $t \approx 17$ mins in the $\lambda-t$ plot of the $H\alpha$ intensity contrast (see Figure 2.2 (g)), and the oscillations began immediately at around $t = 18$ mins persisting until the end of our observation period or even more. Note that weak oscillations are present even before the downflow event, but they are strongly enhanced after the downflow event. The oscillations are conspicuous in the Ca II and Mg II lines, and they are even clearer in the Ca II $\lambda-t$ plot of intensity contrast (see Figure 2.2 (f)). Additionally, the intensity of each line slightly increased after the downflow event, as can be seen in the $\lambda-t$ plots of the Ca II, Mg II, C II and Si IV lines, and more evident in the $\lambda-t$ plot of the Ca II and $H\alpha$ intensity contrast. It suggests that the downflow event caused the oscillations and the associated heating in this region.

Figure 2.3 shows the temporal variations of the LOS Doppler velocity at the same position. The downflow is identified in the $H\alpha$, C II and Si IV lines in common, but the temporal variations of the Doppler velocity are different in each of the lines. In the $H\alpha$ line, the downflow event began at $t = 10$ mins, and the Doppler velocity of the downflow gradually increased reaching its peak value of 7.4 km s^{-1} at $t = 16.5$ mins. Meanwhile, in the C II and Si IV lines, the event began at $t = 14$ mins and the Doppler velocity sharply increased reaching their peaks at $t = 16$ mins with values of 17.4 km s^{-1} and 24.7 km s^{-1} , respectively. We expect the true Doppler velocity of the downflow may be a little higher than these values since the single Gaussian fits may include stationary component as well.

We find several properties of the oscillations that occurred after the downflow event from Figure 2.3. The oscillations are seen in all of the lines, and it implies that the oscillations are detected in a wide range of temperature, i.e., from the chromosphere temperature (10^4 K) to the middle TR temperature ($10^{4.9} \text{ K}$). The amplitude of the oscillations is about 2 km s^{-1} in most of the lines and slightly decreases with time. From the wavelet analysis of power spectrum (Torrence & Compo 1998), we find that the dominant period of the oscillations is initially 2.7 minutes and gradu-

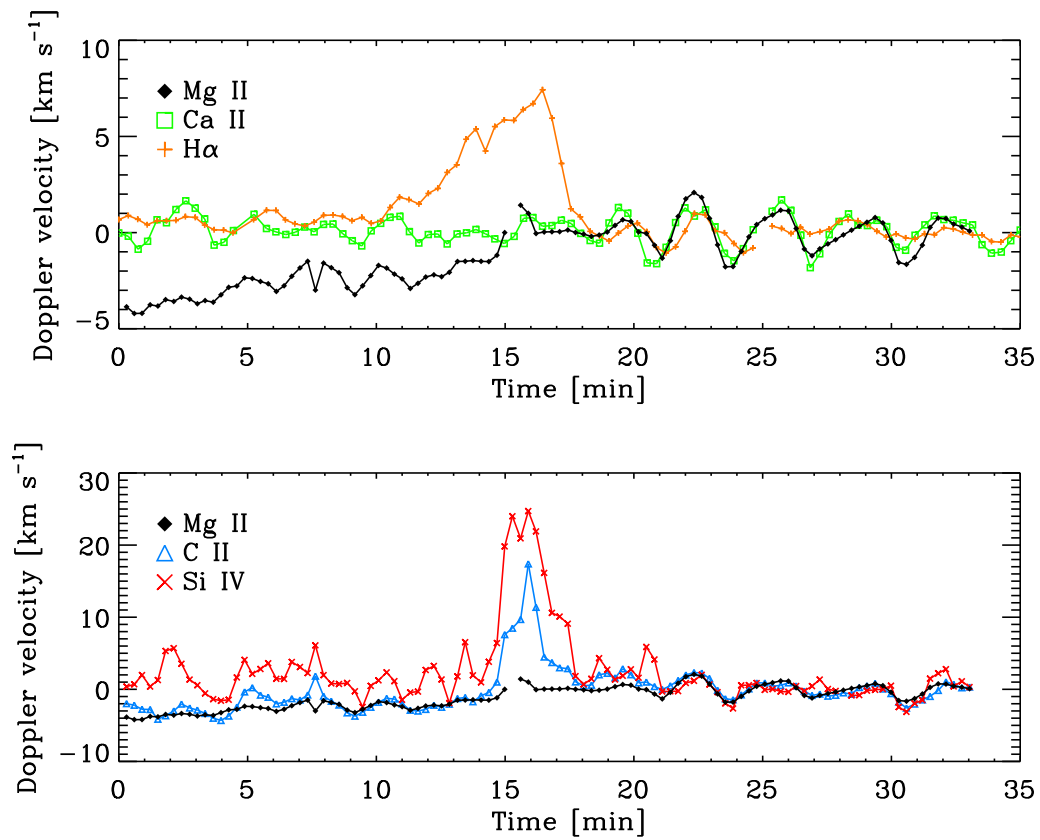


Figure 2.3 Temporal variations of the LOS Doppler velocity in the Ca II, H α and Mg II lines (upper panel), and in the Mg II, C II and Si IV lines (lower panel). Time $t = 0$ corresponds to 17:03:40 UT.

ally increases to 3.3 minutes. These properties of the oscillations are well identified in the Mg II line, and other lines as well. In the case of the Ca II and C II lines, the oscillation patterns are very similar to those of the Mg II line. The Si IV line also shows the same oscillations, but the oscillation patterns are less conspicuous in the Si IV line. The amplitude of the H α Doppler velocity appears smaller than that of the other four lines which may be because the lambdameter method underestimates Doppler velocity of features in the upper chromosphere. Nevertheless, we can still identify the oscillation patterns in the H α line.

Another interesting phenomenon is the coherency of the LOS Doppler velocity patterns in the five different spectral lines after the downflow event (see Figure 2.3). Before the event, each line shows its common velocity reflecting Doppler velocity at each line formation temperature. For example, in the Mg II line, upward motion is dominant and in the Si IV line downward motion is dominant. After the event, however, every line shows a similar pattern of the Doppler velocity. The amplitudes of each line are almost the same and there are no clear phase differences among the five spectral lines.

In Figure 2.4, the downflowing plasma is identified in the H α +0.5 Å image, and we find associated transient brightening in the IRIS SJI 1330 Å. In the H α +0.5 Å image, we can see an elongated absorption feature in the center of the image. The feature is also prominent in the H α LOS velocity map with positive velocity. As seen in the H α +0.5 Å image and the LOS velocity map, the downflow plasma is coming from the outer part of the sunspot to the umbra. During the downflow event, a brightening is identified in the IRIS SJI 1330 Å marked with a white arrow. The brightening corresponds to the end of the H α flow, and the size of the brightening is about 3 ". As seen in the Figure 2.2 (d), the bright feature lasted about three minutes.

On the other hand, there is no associated brightening in the EUV images. In

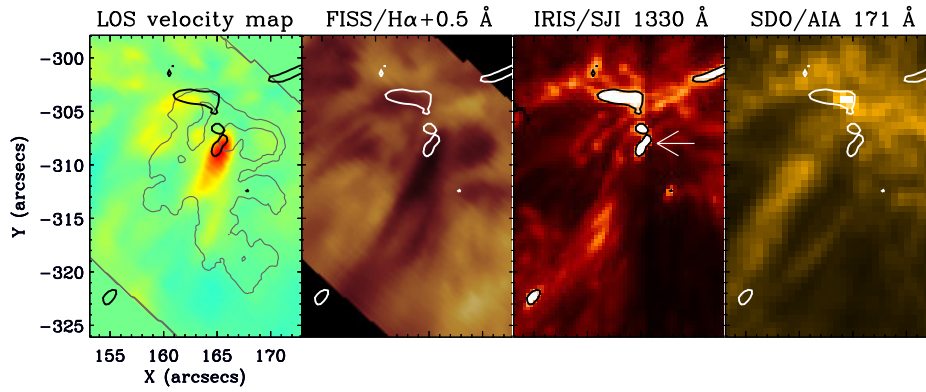


Figure 2.4 Images of the FISS $H\alpha$ LOS Doppler velocity map, $H\alpha+0.5 \text{ \AA}$, IRIS SJI 1330 \AA and AIA 171 \AA during the strong downflow event at around 17:19 UT ($t = 16$). The color of the $H\alpha$ LOS Doppler velocity map is scaled in the range of -8 km s^{-1} (blue) to 8 km s^{-1} (red). Thick contours on each image represent brightenings in the IRIS SJI 1330 \AA , and thin gray contours on the LOS Doppler velocity map indicate the outer boundary of sunspot umbra and penumbra obtained from the FISS/ Ca II-4 \AA image.

the *SDO/AIA* 171 Å images in Figure 2.4 and other EUV images, we cannot find any cospatial and cotemporal brightening associated with the flow identified in the $H\alpha+0.5$ Å image. This means that the temperature of the plasma downflowing along the magnetic fields is not enough to emit EUV light. As a matter of fact, we find a dark elongated feature which is located on the position of the $H\alpha$ flow, and it also corresponds to the elongated bright features in the IRIS SJI 1330 Å.

2.4 Discussion

For the first time, we detected impulsively generated three-minute oscillations above a sunspot in the chromospheric and TR lines. These oscillations are distinct from the three-minute umbral oscillations which exist persistently (e.g., Brynildsen et al. 1999). The oscillations we detected were driven by a strong downflow event above a sunspot. The downflow event suddenly appeared in the $H\alpha$, C II and Si IV lines, and then the oscillations were identified in all of the lines. The amplitudes of the Doppler velocity oscillations were about 2 km s^{-1} , and gradually decreased with time. In addition, the oscillation period was initially 2.7 minutes, and gradually increased to 3.3 minutes. Note that the Doppler velocity oscillations showed a similar behavior in all of the lines after the downflow event. That is to say, the amplitudes of the oscillations were the same values, and there were no evident phase differences among the five lines. We also found that a transient brightening in the IRIS SJI 1330 Å image corresponds to the footpoint of the downflowing material shown in the $H\alpha+0.5$ Å image.

The characteristics of the downflowing material are similar to those of sunspot plumes to a certain degree. Sunspot plumes are generally located above sunspots and have downflows of $20\text{--}30 \text{ km s}^{-1}$ (Maltby et al. 1999; Brynildsen et al. 2001; Brosius 2005). They flow from outside the sunspots toward the umbrae due to gas pressure difference (Doyle & Madjarska 2003). In addition, it has been reported that plumes

are identified in EUV lines formed at TR temperatures of $5.2 \leq \log T(\text{K}) \leq 5.9$ (Brosius 2005). However, the downflowing material we observed is found in the $\text{H}\alpha$ line and only the footpoint part of the material is identified in the FUV line of IRIS SJI 1330 Å. Since the downflowing material is identified in the $\text{H}\alpha$ line and not in the EUV lines, it may imply that the temperature of the material is lower than that of the typical sunspot plumes.

We conjecture that the three-minute oscillations we observed represent gravity-modified acoustic waves generated by an impulsive disturbance (Lamb 1909; Kalkofen et al. 1994; Chae & Goode 2015). The well-known work of Fleck & Schmitz (1991) demonstrated that three-minute oscillations arise as a natural response of the atmosphere excited by a five-minute piston motion in the lower boundary. Chae & Goode (2015) regarded this phenomenon as a consequence of the sudden set-up of the driving motion which is a sort of impulsive disturbance from the initial equilibrium. According to Chae & Goode (2015) an impulsive disturbance in a gravitationally stratified medium generates two packets of dispersive acoustic waves, i.e., high frequency waves and low frequency waves. Since the group speeds of the high frequency waves are higher than those of the low frequency waves, they propagate faster than the low frequency waves. For this reason, at a fixed position, the observed oscillation frequency changes from high to low values, or the oscillation period changes from short to long values. In addition, since the waves carry energy away, the amplitude of the oscillations decreases with time. These theoretical characteristics are consistent with our findings of the occurrence of the oscillations, the increase of the oscillation period and the decrease of the oscillation amplitude. Indeed, the waves generated in a gravitationally stratified medium are dispersive, and they propagate out of the source region (Kalkofen et al. 1994; Chae & Goode 2015). Thus, there should be a phase difference of the velocity oscillations when they are observed in two different atmospheric layers. Additionally, the amplitudes of the velocity oscillations may be

different in the two different layers, since they are affected by physical conditions of the layer which they belong to.

One may wonder why the oscillations in our data show a similar behavior in all of the chromospheric (Ca II, H α , Mg II) and the TR lines (C II, Si IV). A possible explanation is that the five spectral lines were formed in the same atmospheric layer. The bright feature seen in the IRIS SJI 1330 Å corresponds to the end of the downflow material. It indicates that the footpoint of the flow rooted in the lower atmosphere (chromosphere) is heated up to middle TR temperatures ($10^{4.9}$ K) probably by the gravitational energy of the material flowing along the flux tube. The TR temperature plasma, however, may be far from ionization equilibrium. Hence all the neutrals and singly-ionized elements will get ionized in a short time because of the enhanced temperature and density (Carlsson & Stein 2002). The TR temperature plasma, however, may still contain some amount of neutrals and singly-ionized elements reproduced by the recombination of ions and electrons. The spectral lines of these species may display the same dynamical property as the other TR lines, and therefore the oscillations we identified in the five spectral lines may show high similarities.

Our results suggest that impulsive events can drive three-minute oscillations in the chromosphere. Among them we observed a transient downflow event that occurred in the chromospheric parts of magnetic loops anchored inside the sunspot. Since the solar chromosphere displays a variety of impulsive events, we expect that all the events may significantly contribute to the generation of oscillations and waves in the solar chromosphere.

Chapter 3

Impulsive Wave Excitation by Rapidly Changing Granules¹

3.1 Introduction

A wide range of observations have revealed that oscillations and waves are abundant in the solar atmosphere. They are clearly observed in the umbral and penumbral regions of sunspots (e.g., Beckers & Schultz 1972) and the network and internetwork regions of the quiet Sun (e.g., Orrall 1966; Deubner & Fleck 1990). It is not yet known how waves are generated in the solar atmosphere. Theoretical studies suggest that solar acoustic waves can be produced by impulsive disturbances in a gravitationally stratified medium (Kalkofen et al. 1994; Chae & Goode 2015). Chae & Goode (2015) report that when a region is disturbed by an impulsive event, acoustic waves with an acoustic cutoff frequency naturally arise in a medium. In terms of global p-mode oscillations, it is now generally accepted that p-modes are excited by turbulent con-

¹Most of the contents in this chapter were written as a separate paper: Hannah Kwak, Jongchul Chae, Maria S. Madjarska, Kyuhyoun Cho, Donguk Song, “Impulsive Wave Excitation by Rapidly Changing Granules”, 2020, A&A

vection (Goldreich & Kumar 1990). Nigam & Kosovichev (1999) found that a wave excitation source is located at a depth of 75 ± 25 km below the photosphere by comparing theoretical and observed p-mode power spectra. Since turbulent convection occurs ubiquitously, the observed oscillations show the superposition of oscillation signals coming from different sources. In this regard, investigating an individual wave excitation event that is well-separated in time and space could facilitate the establishment of the wave excitation process.

The wave excitation process appears to be related to localized disturbances below the photosphere. Using one-dimensional simulations, Goode et al. (1992) showed that acoustic waves are excited by individual wave excitation events occurring less than 200 km below the base of the photosphere. Rimmele et al. (1995) found a spatially localized transient wave energy flux that arises due to the excitation of waves beneath the photosphere. These phenomena are termed acoustic events and they are generally found in the intergranular lanes (Rimmele et al. 1995; Bello González et al. 2010). On a much larger scale, they are found in intergranular lanes located in or near the boundaries of regions with predominant downward vertical motions and horizontal converging flows on a mesogranular scale (Malherbe et al. 2015). Before the acoustic events occur, darkening of intergranular lanes is observed at the photospheric level, and the darkening is interpreted as catastrophic cooling that occurs in the intergranular lanes below the photosphere (Rimmele et al. 1995). Similarly, theoretical studies suggest that localized cooling events and subsequent downflows could be related to a wave excitation process (Rast 1999; Skartlien et al. 2000).

Furthermore, the waves generated beneath the photosphere propagate upward and affect the upper atmosphere. In the internetwork region, small intermittent brightenings have been observed in Ca II H and K filtergrams and time series of spectra (e.g., Bappu & Sivaraman 1971; Zirin 1974; Cram & Dame 1983). These brightenings are called Ca II bright grains or internetwork grains, and several studies have

suggested that they are closely related to wave phenomena due to their recurrent behavior (for a review, see Rutten & Uitenbroek 1991). Based on one-dimensional non-local thermodynamic equilibrium (non-LTE) radiation-hydrodynamic simulations, Carlsson & Stein (1997) asserted that the bright grains are produced by waves coming from below the photosphere that subsequently develop into acoustic shocks in the mid-chromosphere (~ 1 Mm above $\tau_{500} = 1$). Several observational studies have shown that most of the chromospheric bright grains coincide with photospheric oscillations and even photospheric darkening events. Hoekzema et al. (2002) reported that sites with the largest acoustic flux (i.e., acoustic events) in the photosphere tend to collocate with chromospheric bright grains with an average time delay of 2 min. Similarly, Cadavid et al. (2003) investigated 1527 G-band darkening events and found that 72% of the photospheric darkenings are followed by Ca II K brightenings with time lags of about 2 min. Using time series of Ca II H, H α , and Fe I spectra, Kamio & Kurokawa (2006) established that the Ca II H bright grains are caused by acoustic shocks in the chromosphere that are associated with enhanced 5 mHz oscillations in the photosphere.

Recently, space-based observations that do not suffer from the atmospheric seeing and cover a large field of view (FOV) permitted the simultaneous identification of numerous acoustic events. Using high-resolution data taken with the Solar Optical Telescope (SOT) on board the Hinode satellite, Malherbe et al. (2012) studied the properties of acoustic events such as acoustic flux, velocity amplitude, continuum intensity, and divergence. They also found that most acoustic events appear in the intergranular lanes in regions with downward velocities and converging motions. Even though general properties of acoustic events are well known from the analysis of large FOV high-resolution data, the wave excitation process of individual acoustic events has not yet been investigated in detail.

In this chapter, we report the excitation of waves by a new type of event: granules

that undergo rapid dynamic changes. These events differ from classic acoustic events. The new acoustic events studied here are caused by granules that experience dynamic changes rather than by events occurring in intergranular lanes. These granules either collapse, fragment, or submerge in the photospheric layer. To understand the wave excitation and propagation, we investigated the temporal behavior of the granules as well as the Doppler velocities in the photospheric and chromospheric layers. We used high-spatial and high-spectral resolution data obtained by the Fast Imaging Solar Spectrograph (FISS; Chae et al. 2013) and high-resolution photospheric data taken with the TiO 7057 Å broadband filter imager (Cao et al. 2010) installed on the 1.6 m Goode Solar Telescope (GST) of the Big Bear Solar Observatory. Our analysis shows a one-to-one correlation between dynamically changing granules and the excitation of acoustic waves.

3.2 Observations and data analysis

The observations were taken on June 14, 2017, in a quiet Sun region with the FISS and the TiO 7057 Å broadband filter imager. The FISS is a dual-band Echelle spectrograph that takes simultaneous H α and Ca II 8542 Å spectrograms with imaging capability. The spatial pixel size is 0''16, and the spectral pixel size is 0.019 Å in the H α band and 0.026 Å in the Ca II band. The FOV, with a size of 24'' \times 40'', is centered at the solar heliographic coordinates X = -140'' and Y = -70''. It was scanned with a cadence of 27 s for one hour, from 17:52:03 to 18:52:13 UT (hereafter the time 17:52:03 UT is referred to as $t = 0$). Detailed information about the instrument and the basic data processing, including the flat-field correction, distortion correction, and noise suppression, is given in Chae et al. (2013).

We acquired photospheric images using the TiO 7057 Å broadband filter imager at 15 s cadence and an exposure time of 0.7 ms. The speckle reconstruction was done with the Kiepenheuer-Institut Speckle Interferometry Package (Wöger et al. 2008)

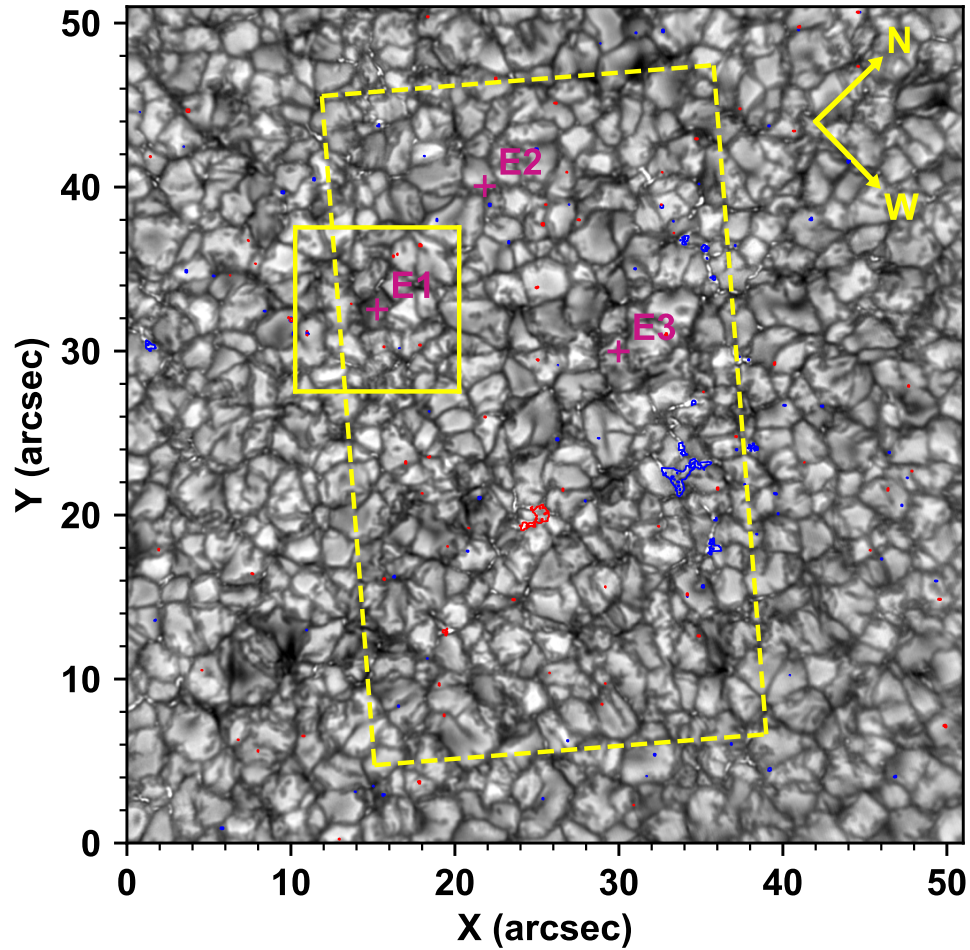


Figure 3.1 Photospheric TiO 7057 Å broadband filter image of a quiet Sun region taken at 18:03:56 UT ($t = 11.9$ min). The dashed yellow line rectangle represents the FOV of the FISS. The small yellow square indicates one of our regions of interest, and the size of the square is $10'' \times 10''$. The locations of each event are marked with purple cross symbols and annotated as E1, E2, and E3. The contours represent the line of sight (LOS) magnetogram obtained from the Near-Infrared Imaging Spectropolarimeter (NIRIS) installed on the GST. The blue and red contours represent LOS magnetic field strengths of -100 G and 100 G, respectively.

to achieve diffraction-limited images. The spatial pixel size is $0''.034$ and the FOV is $70'' \times 70''$. Figure 3.1 shows the TiO image taken at 18:03:56 UT ($t = 11.9$ min). The observed region includes an internetwork region and some magnetic elements that are considered to be part of the network region. The TiO and the FISS data were aligned using the TiO and the FISS $H\alpha-4 \text{ \AA}$ raster images.

We obtained the line-of-sight Doppler velocities using the lambda-meter method (Deubner et al. 1996). We set $\Delta\lambda$ and determined the λ_m that satisfies the equation $I(\lambda_m - \Delta\lambda) = I(\lambda_m + \Delta\lambda)$. Since the $H\alpha$ and $\text{Ca II } 8542 \text{ \AA}$ bands also include photospheric lines such as $\text{Ti II } 6560 \text{ \AA}$ and $\text{Si IV } 8536 \text{ \AA}$, we could also measure the photospheric velocities. In this study, the $\text{Ti II } 6560 \text{ \AA}$ and $H\alpha$ lines were used to infer the photospheric and chromospheric velocities, respectively. In addition, we only obtained velocity signals with periods from 1 to 6 min by applying a bandpass filtering method based on the wavelet analysis given by Torrence & Compo (1998), which eliminates the solar granulation pattern corresponding to an approximately 10 min period and noise. The bandpass filter we applied is found to be broad enough not to lose any of the acoustic events' power.

In a wavelet analysis, it is important to use an appropriate background noise model for detecting significant oscillatory power. To evaluate the background noise model from the FISS data, we took a $16'' \times 32''$ area of the central region from the $H\alpha$ and Ti II data and obtained spatially averaged Fourier power spectra, which are regarded as the background noise model $\sigma(\nu)$. The Fourier power spectra were modeled using the following combination of a power law function and a Gaussian function:

$$\sigma(\nu) = A\nu^s + B \exp\left(-\frac{(\nu - \nu_0)^2}{\sigma_G^2}\right). \quad (3.1)$$

The model has five parameters for each line. The inferred parameters are $A = 0.02$, $s = -0.79$, $B = 7.1$, $\nu_0 = 4.3 \times 10^{-3} \text{ Hz}$, and $\sigma_G = 3.9 \times 10^{-3} \text{ Hz}$ for $H\alpha$, and $A = 2.1 \times 10^{-5}$, $s = -1.5$, $B = 0.66$, $\nu_0 = 3.6 \times 10^{-3} \text{ Hz}$, and $\sigma_G = 9.0 \times 10^{-4} \text{ Hz}$ for

Ti II. The results of the noise model fitting are shown in Figure 3.2. Figure 3.2 shows the Fourier power spectra and noise models for the H α and Ti II data. The models consist of a power law and a Gaussian term. We note that the white noise term as measured by the value of C is negligible in both cases. Using this information, we calculated the 95 % local confidence level for both data (see Figure 3.9 (d) and (e)) following Auchère et al. (2016) and Kayshap et al. (2020). We note that the noise model considered here is not for measurement errors, but for the background signals commonly seen in the data. The Gaussian component in this noise model represents the 5 min p-mode oscillations. Therefore, the events above a significance level are those that have much stronger power than the p-modes.

The wave energy flux is calculated within the 3 min band (2 to 4 min) at each spatial pixel by following the method and assumptions given in Chae et al. (2017). We assumed that the acoustic waves propagate vertically in a gravitationally stratified medium (from the photosphere to chromosphere) and that the medium is isothermal. Since waves, in reality, may propagate in the non-vertical directions as well, only some part of the total energy may be carried vertically, and the energy flux in the chromosphere may be smaller than that in the photosphere. Therefore, we estimated the wave energy flux in the photospheric level. The photospheric wave energy flux is given by the expression

$$F_w = U_1 v_g = \rho_1 P_{\nu,1} \frac{c_s^2}{v_p} = \rho_1 P_{\nu,1} \frac{c_{s,1} c_{s,2}}{v_p}, \quad (3.2)$$

where U is the wave energy density, v_g is the group velocity, ρ is the mass density, P_{ν} is the 3 min band oscillation power, c_s is the sound speed, and v_p is the phase velocity. The photospheric and chromospheric parameters are denoted by 1 and 2, respectively. We determined the group velocity v_g from the phase velocity v_p using the relationship of $v_g v_p = c_s^2$, which is applicable to acoustic waves. The phase

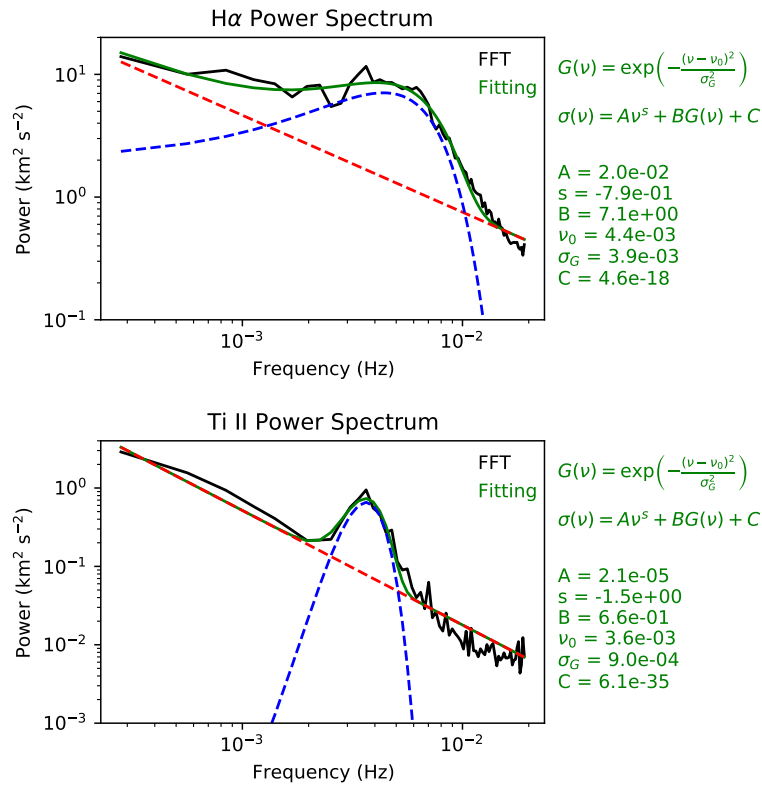


Figure 3.2 Fourier power spectra and noise models for the H α (upper panel) and Ti II (lower panel) data. In each panel, the solid black line represents the Fourier power spectra and the solid green line represents their model fitting results. The dashed red and blue lines indicate the power law and Gaussian term, respectively.

velocity v_p can be expressed as

$$v_p = \frac{\omega}{k} = \omega \frac{\Delta z}{\Delta \Phi}, \quad (3.3)$$

where ω is the frequency, k is the wavenumber, $\Delta \Phi$ is the phase difference, and Δz is the height difference. The value of $\Delta \Phi$ is acquired from the wavelet analysis by computing the phase difference between the velocity time series of the Ti II and H α lines. The height difference Δz is determined from the formation height of the Ti II and H α lines. To infer the formation height of the Ti II line, we assumed that the Ti II line and continuum are formed under local thermodynamic equilibrium (LTE) conditions. Thus, the intensity ratio between the Ti II line core and the continuum can be substituted for their temperature ratio. The continuum is formed at 0 km, and the temperature value of 6520 K is adopted from the FALC model (Fontenla et al. 1993). From the intensity ratio between the Ti II line core and the continuum, we determined the formation height of the Ti II line as 75 km, where the temperature is 5580 K. We assumed the formation height of the H α line core to be 1.5 Mm (Vernazza et al. 1981; Leenaarts et al. 2012). For the mass density and sound speed, we also used values from the FALC model at the specific heights.

3.3 Results

We identified wave excitation events related to granules undergoing dynamic changes. These granules collapse, fragment, or submerge. Subsequently, velocity oscillations are detected in the photospheric and chromospheric layers. In Figure 3.1, we show the locations of three of them (hereafter event 1, event 2, and event 3) that were investigated in detail. Event 1 is associated with a collapsing granule, event 2 with a fragmenting one, and event 3 with a submerging one.

3.3.1 Dynamically changing granules

Event 1 represents a case of a granule that became considerably dark with an edge collapsing within 5 min. Initially ($t = 6.1$ min), in the center of the TiO image, the brightness of the granule was similar to that of the surrounding region, but after 2.5 min the entire granule began to darken (see Figure 3.3). The granule reached its minimum intensity at $t = 13.6$ min; the intensity was particularly low at the east edge (yellow arrow in Figure 3.3). After the collapse, the size of the granule slightly decreased. After $t = 13.6$ min, the granule progressively became brighter and at $t = 16.2$ min returned to its initial brightness. The same granule is also seen in the $\text{H}\alpha$ -4 Å images, but, due to the limitation of the spatial resolution, the detailed dynamic changes of the granule cannot be followed. The dynamic changes are just seen as a darkening. Likewise, these darkenings are identified in the $\text{H}\alpha$ -4 Å images of events 2 and 3 (lower panels of Figs. 3.4 and 3.5).

Figure 3.4 shows the time series of event 2, which represents an expanding granule that later splits into two granules. The brightness of the expanding granule is lower than the neighboring granules. At $t = 3.1$ min, the center of the granule became darker (yellow arrow in Figure 3.4), while the granule kept expanding with time. At the location where the darkening occurred, the granule split into two individual granules ($t = 6.1$ min).

In the time series of event 3 (Figure 3.5), we find two submerging granules (yellow arrows in Figure 3.5). Before the submergence ($t = 20.6$ min), these two granules were located (cyan arrows) between the continuously expanding granules (see the time series of TiO images). The two granules shrank with time, whereas surrounding granules kept expanding. Eventually, at $t = 30.7$ min, the small granules submerged and the sites remained as typical intergranular lanes.

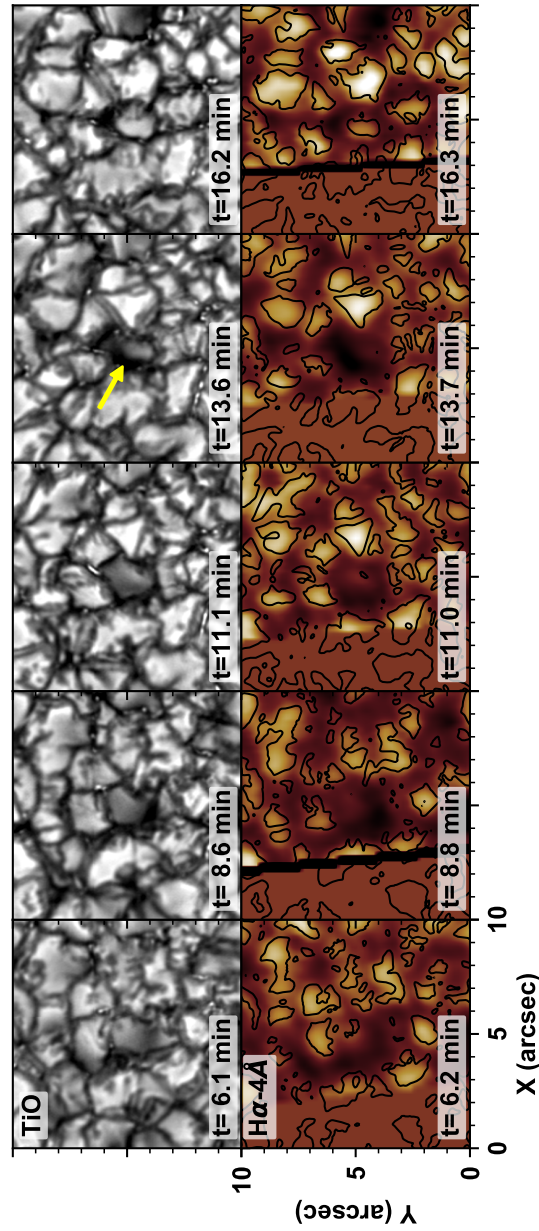


Figure 3.3 Temporal evolutions of the granule of event 1 in the TiO images (upper panel) and the H α -4 Å raster images (lower panel). The contours on the H α -4 Å raster images represent the granules obtained from the TiO images. The yellow arrow indicates the position where the dynamic changes of the granule occurred.

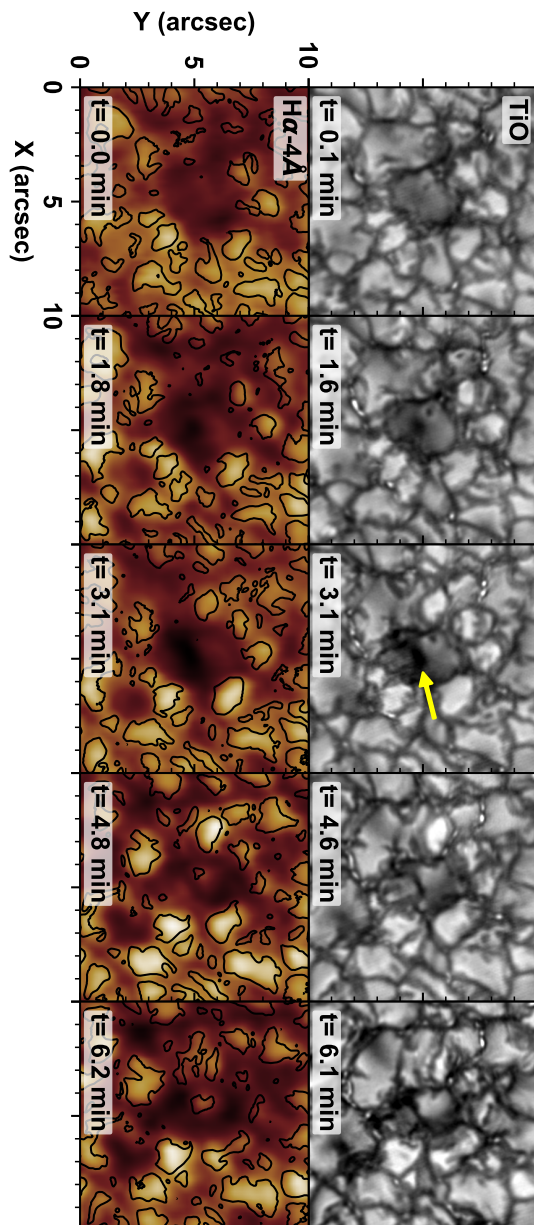


Figure 3.4 Same as Figure 3.3, but for event 2.

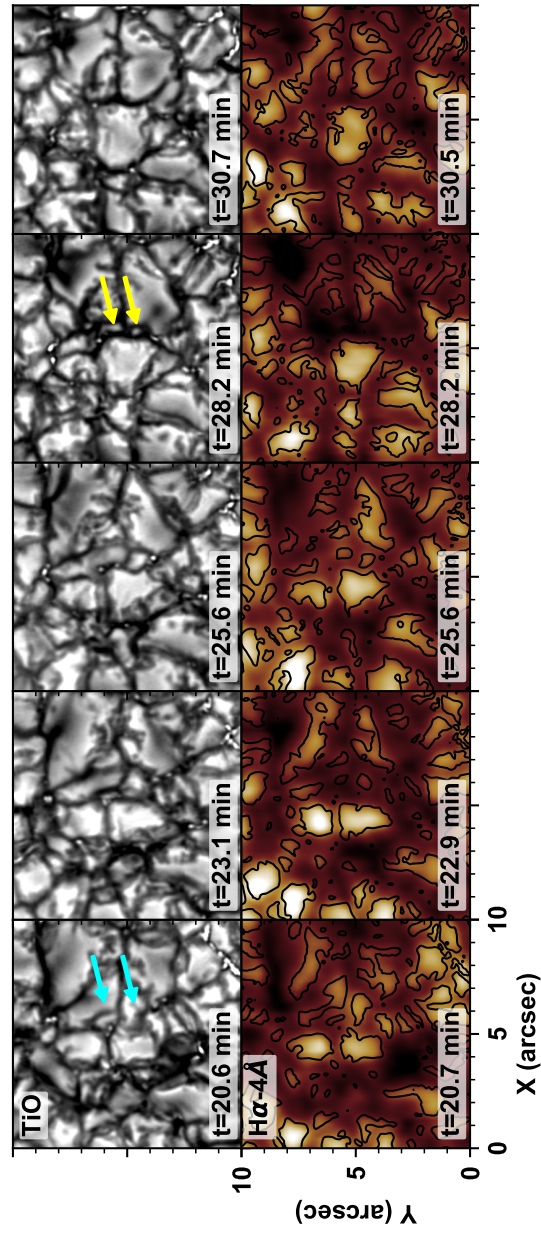


Figure 3.5 Same as Figure 3.3, but for event 3. The cyan arrows indicate the initial positions of the submerging granules.

3.3.2 Wave excitation

Shortly after the dynamic changes of each granule, oscillations are clearly identified in the photosphere and chromosphere. Figure 3.6 shows the time series of the photospheric images and the Doppler maps of event 1. When the darkening becomes intense ($t = 13.6$ min), the oscillation pattern begins in the Ti II Doppler maps. A downward velocity patch (red-colored) appears abruptly above the darkening granule and is immediately followed by an upward velocity patch (blue-colored). For a while, downward and upward velocity patches appear in turns. The oscillation pattern lasts approximately 10 min. The spatial size of the oscillation pattern is approximately $3''.5$, which is slightly bigger than the size of the granule. A similar oscillation pattern with enhanced amplitude is identified in the H α Doppler maps, but the shape of the oscillation patch is slightly different compared to that in the Ti II Doppler maps. This discrepancy is not surprising because the photosphere and the chromosphere are not necessarily connected by vertical magnetic fields. The magnetic configuration is usually complex in quiet regions, and the chromosphere is often permeated by highly inclined magnetic field lines.

Likewise, in events 2 and 3, photospheric and chromospheric oscillations are detected above the fragmenting (Figure 3.7) and submerging (Figure 3.8) granules. In the Ti II Doppler maps, the locations of the velocity patches coincide exactly with those of the changing granules. However, the shapes of the velocity patches are less obvious compared to event 1, probably because of the non-vertical magnetic configuration as described above. Also, the amplitudes of the oscillations are smaller. Therefore, it is difficult to distinguish the oscillation pattern from the surrounding velocity patterns that are not related to the dynamically changing granules. In the H α Doppler maps, the oscillation pattern is hard to notice. Thus, event 1 shows the best isolated oscillation pattern in both the photospheric and the chromospheric Doppler maps. We chose this event for further analysis.

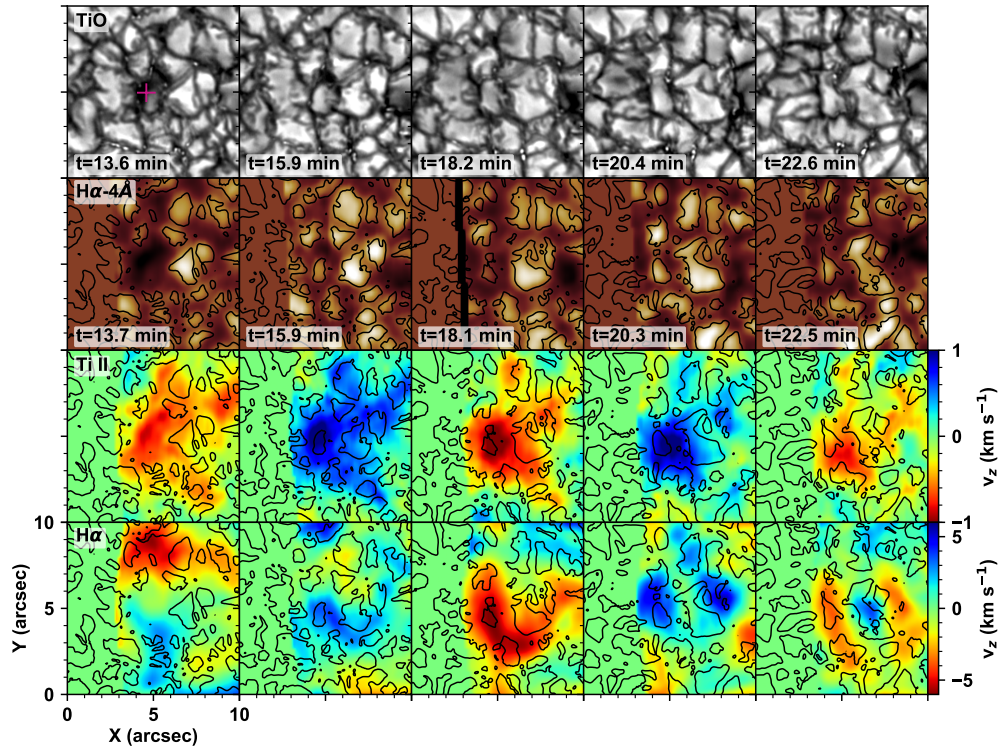


Figure 3.6 Time series of the TiO images (first row), $H\alpha-4\text{ \AA}$ raster images (second row), and vertical velocity maps of the Ti II (third row) and $H\alpha$ (fourth row). The contours on the $H\alpha-4\text{ \AA}$ raster images and the vertical velocity maps indicate the granules obtained from the TiO images. A purple cross symbol in the first TiO image ($t = 13.6\text{ min}$) marks the selected position that was further analyzed and is shown in Figs. 3.9 and 3.10.

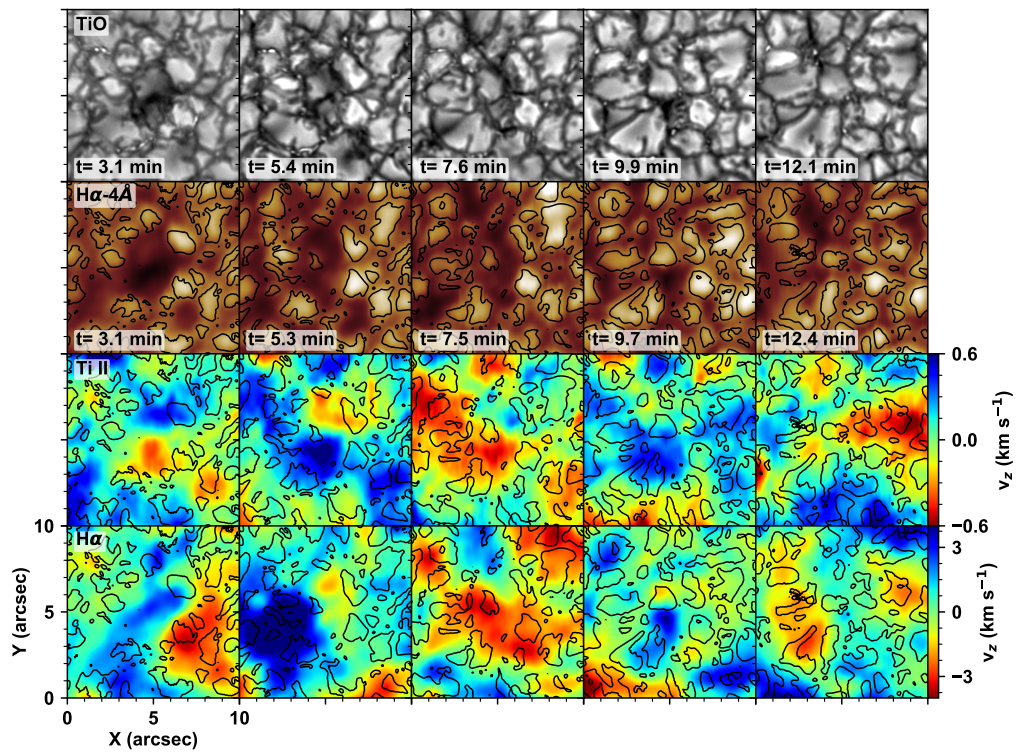


Figure 3.7 Same as Figure 3.6, but for event 2.

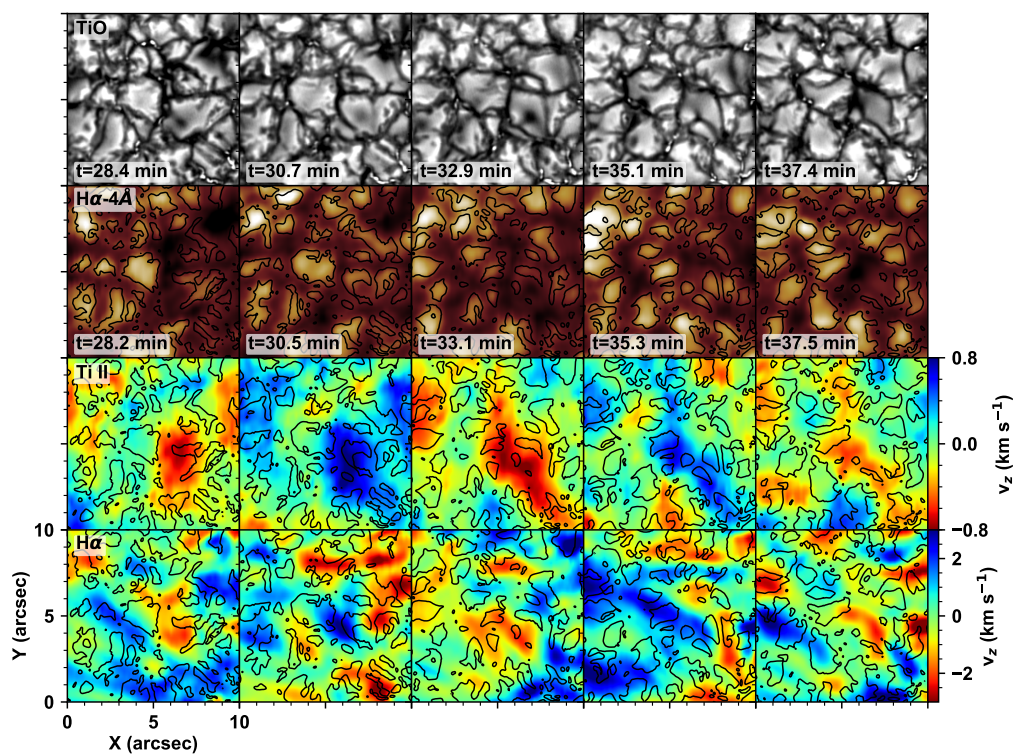


Figure 3.8 Same as Figure 3.6, but for event 3.

Figure 3.9 presents the temporal variations of the intensity and the velocities of event 1. The TiO intensity and the vertical velocities of the Ti II and H α lines are obtained from a selected position in Figure 3.6. The position is chosen because it is the location at the dark edge of the granule that has the highest photospheric velocity. As mentioned above, the intensity of the granule is close to the spatially averaged value of the intensity at the start of the event. A few minutes later, it starts to gradually decrease in time. The intensity reaches its minimum value at $t = 13.6$ min. For 13.6 min, the intensity decreases by about 12%. Then, the intensity rapidly increases to a value even higher than the initial value.

The velocity oscillations are identified in the time series of 1–6 min bandpass-filtered velocities. In the Ti II line, just before the intensity minimum, the oscillations start with a downward motion. The amplitude of the oscillations is approximately 1 km s^{-1} . The corresponding wavelet power spectrum indicates that the power of the oscillations is mostly concentrated in the range of 3 to 6 min, and the dominant period of the oscillations is 4.2 min. In the H α line, the amplitude of the oscillations is about 5 km s^{-1} , and the power is concentrated in a similar range but includes more short-period components than that of the Ti II line. The dominant period of the H α velocity oscillations is 3.8 min.

We calculated the wavelet coherency and phase difference of the velocities measured at two different layers. The coherency becomes higher when the granule is sufficiently darkened ($t \sim 10$ min), especially in the 4 to 6 min period range. In the case of 3 to 4.5 min period waves, the phase differences are at approximately 0.35–0.5 rad, which indicates an upward propagation of the waves. In the longer period regime (> 4.5 min), the phase differences are close to zero or have negative values. This indicates standing waves or downward propagating waves. It is considered to be a natural consequence since the longer period waves, which are longer than the cutoff period, cannot go through the chromosphere.

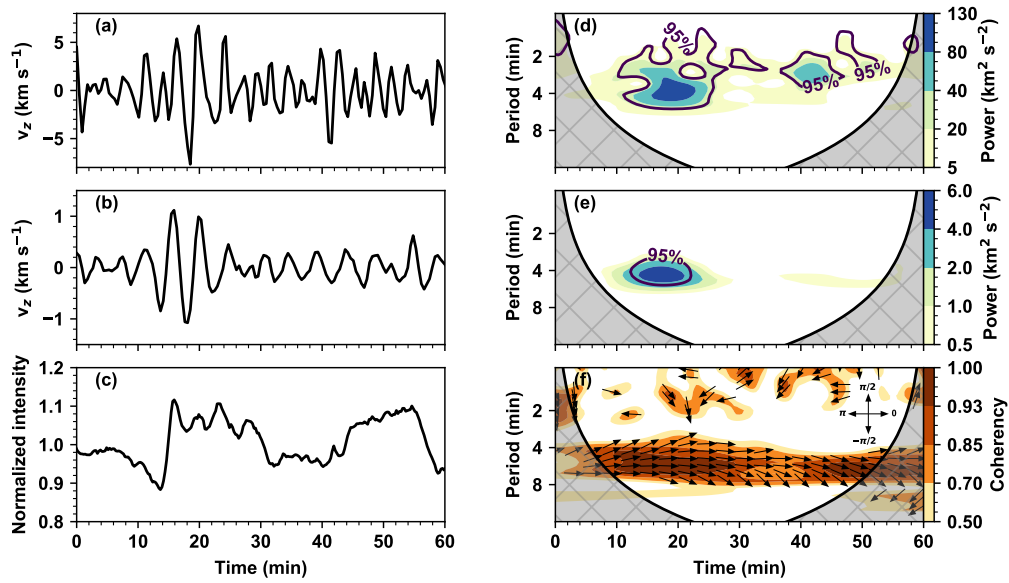


Figure 3.9 Left: temporal variations of the H α vertical velocity (a), Ti II vertical velocity (b), and TiO intensity (c) at the position marked with a cross symbol in Figure 3.6. Right: wavelet power spectra of H α vertical velocity (d) and Ti II vertical velocity (e). The purple contours represent the 95% local confidence level. The coherency between the two time series of velocity is shown by contours in (f). The phase differences at the points of coherency above 0.7 are denoted by the directions of the arrows.

3.3.3 Wave propagation and influence on the higher atmosphere

During event 1, upward wave energy flux is enhanced during the photospheric and chromospheric velocity oscillations (see Figure 3.10). We measured the wave energy flux integrated over the periods from 2 to 4 min (3 min band) in the photospheric layer. The upward wave energy flux is conspicuous above the granule that underwent darkening. The spatial size of the flux patch is larger than that of the granule. Next to the wave energy flux patch that we are interested in, there is another wave energy flux enhancement that is even larger and located in the intergranular lanes. It represents another wave excitation event related to converging flows that cause some granules to submerge. The lower figure shows the temporal variation of the wave energy flux at the selected position in Figure 3.6. The flux is on the order of $10^6 \text{ erg s}^{-1} \text{ cm}^{-2}$ and the peak value is $9.6 \times 10^6 \text{ erg s}^{-1} \text{ cm}^{-2}$ at $t = 15.4 \text{ min}$.

At this point, we compare our acoustic events and regular acoustic waves (p-mode oscillations). The oscillations during the time interval $t = 30$ to 40 min (see Figure 3.9) are identified with the regular acoustic waves. The velocity oscillations during this time interval have smaller amplitudes in both the $\text{H}\alpha$ and Ti II vertical velocity plots and have the phase differences that are close to zero or negative values, meaning that they are standing waves or downward propagating waves. As expected, the wave energy flux is close to zero (see Figure 3.10). Therefore, regular acoustic waves cannot transfer energy upward and are distinct from the waves excited by rapidly changing granules.

After the granule darkens ($t = 13.6 \text{ min}$), repetitive brightenings are identified in the Ca II-0.5 \AA raster images (see Figure 3.11). The brightenings occurred at $t = 15$ and 19 min , and the time interval ($\sim 4 \text{ min}$) is close to the dominant period of the chromospheric oscillations that were inferred from the $\text{H}\alpha$ line. The brightenings are more prominent above the intergranular lanes. The right panel of Figure 3.11 shows the wavelength-time ($\lambda - t$) plot of the Ca II 8542 \AA line acquired above the bright-

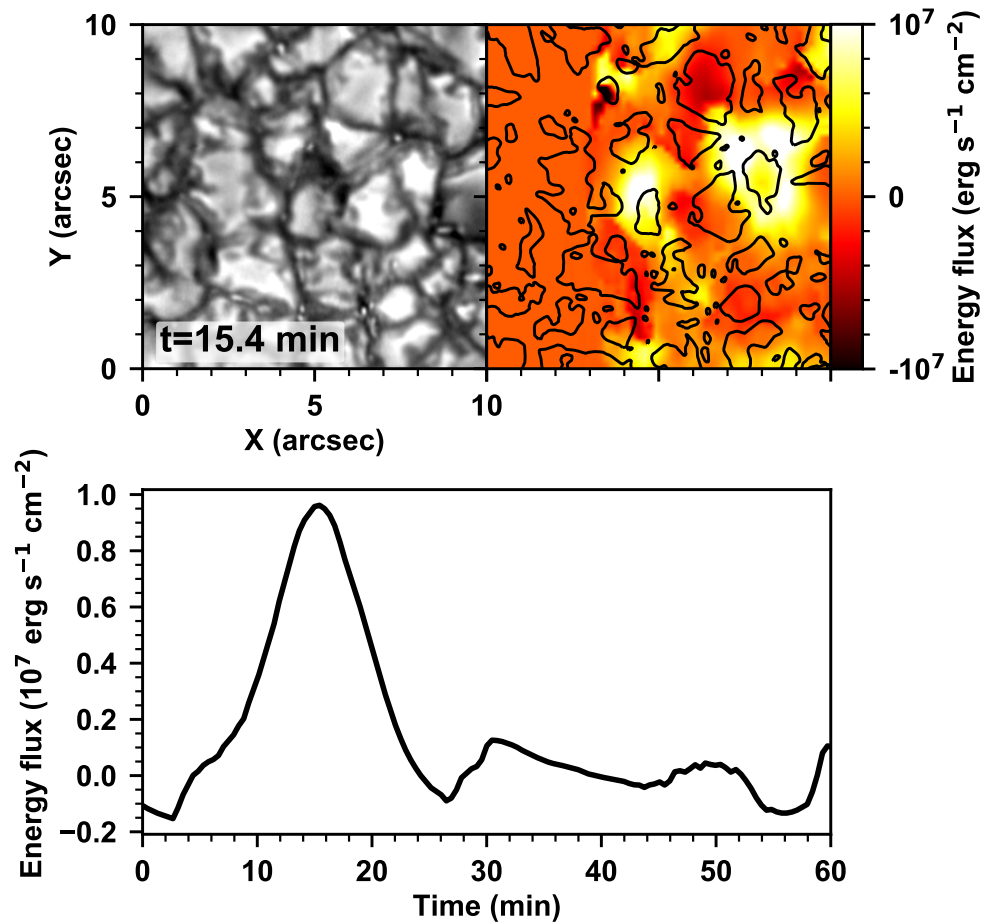


Figure 3.10 TiO image (top left) and photospheric wave energy flux map (top right) at $t = 15.4$ min. The contours on the wave energy flux map indicate the granules obtained from the TiO images. The temporal variation of the wave energy flux (bottom) is acquired at the position marked with a cross symbol in Figure 3.6.

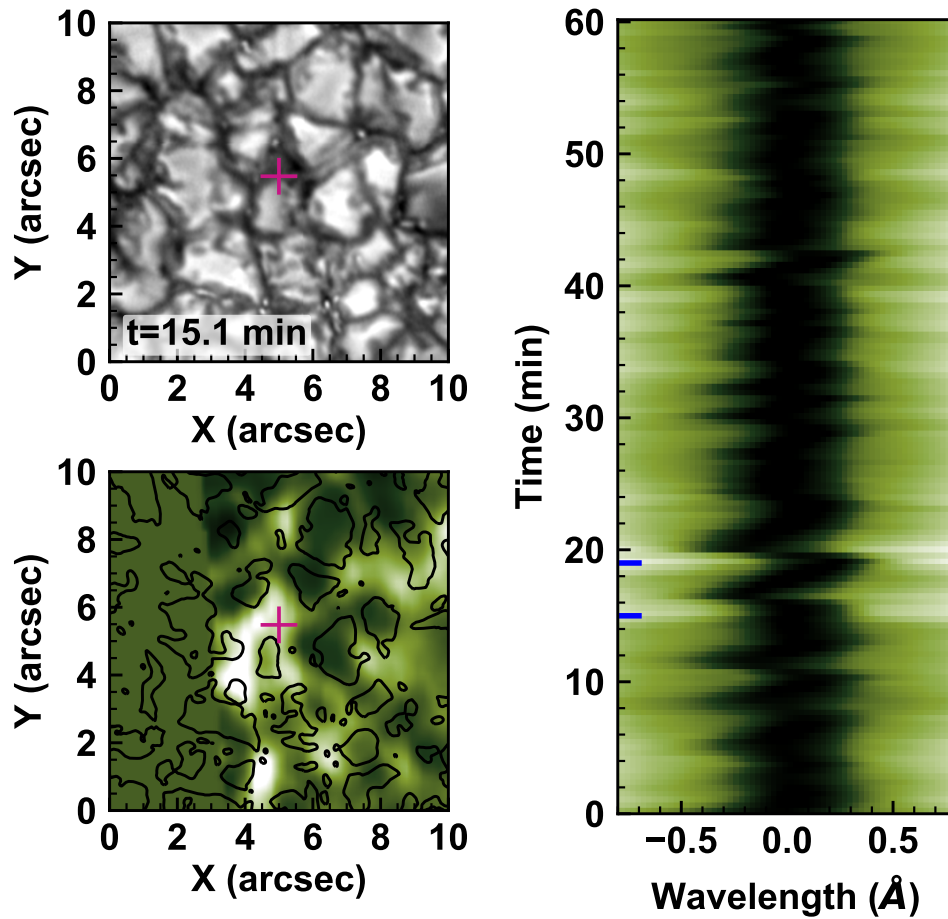


Figure 3.11 TiO image (top left) and the Ca II-0.5 Å raster image (bottom left) at $t = 15.1$ min. The wavelength-time ($\lambda - t$) plot of the Ca II 8542 Å line intensity (right) was taken from the position marked with a purple cross symbol on the Ca II-0.5 Å raster image. In the $\lambda - t$ plot, two brightenings are marked with blue horizontal lines at $t = 15$ and $t = 19$ min.

enings. The collapsing granule event occurred at $t = 13.6$ min, and two brightenings can be identified at $t = 15$ and 19 min. The duration of each brightening is about 2 min. The temporal behavior of the brightenings is consistent with previous studies of Ca II bright grains (Cram & Dame 1983; Kamio & Kurokawa 2006). In addition, we can clearly see the sawtooth pattern, which is known as the manifestation of shock waves.

3.3.4 Classic acoustic event

Figure 3.12 shows the time series of the photospheric and the Doppler maps of a classic acoustic event. At $t = 6.6$ min, a darkening of intergranular lanes is identified in the photospheric images. It is obvious in the $H\alpha$ -4 Å raster image. At the same time, an oscillation pattern starts with a downward velocity patch in the Ti II and $H\alpha$ vertical velocity maps, and the pattern lasts about 10 min. Since the oscillation pattern is confined to the intergranular lanes, the spatial size of the oscillation pattern is smaller than that of the new-type acoustic events reported here. The dominant periods of the oscillation are 4 min at the photospheric level and 3.9 min at the chromospheric level. The wave energy flux above the intergranular lanes is on the order of 10^6 erg s⁻¹ cm⁻². The maximum value is 3.6×10^6 erg s⁻¹ cm⁻².

3.4 Discussion

We have reported the excitation of waves above dynamically changing granules in the internetwork region of the quiet Sun. Three dynamically changing granules that collapse (event 1), fragment (event 2), or submerge (event 3) are studied in detail. Above these granules, spatially localized and transient velocity oscillations are detected in the photospheric and chromospheric layers. In the case of event 1, the dominant periods of the oscillations are 4.2 min and 3.8 min in the photosphere and chromosphere,

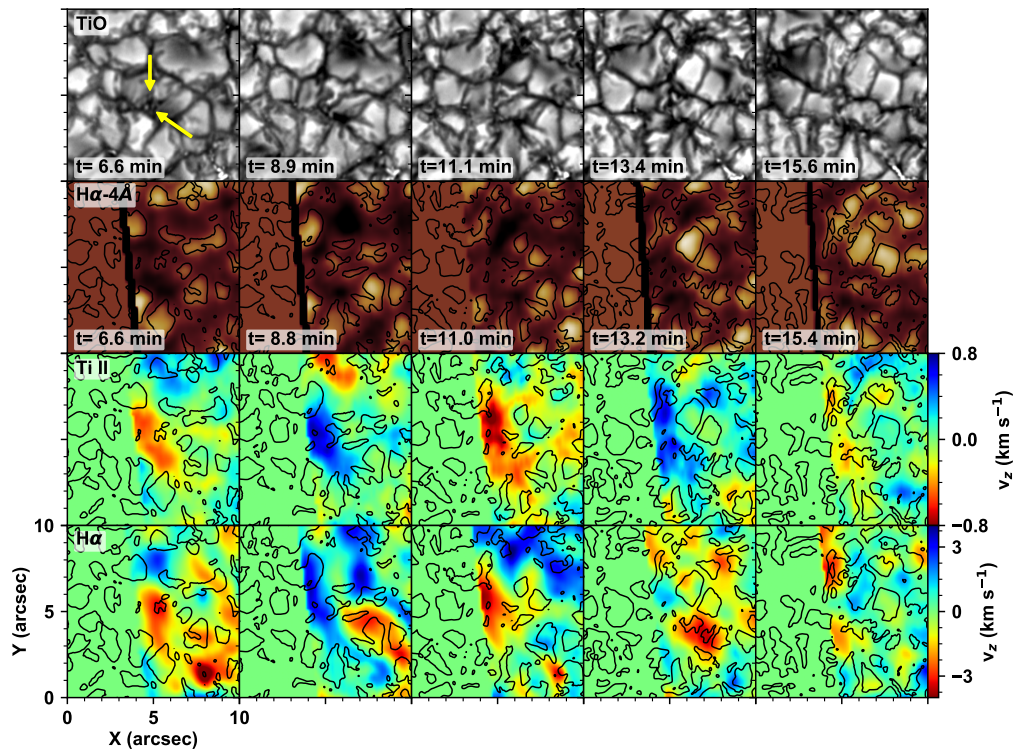


Figure 3.12 Same as Figure 3.6, but for a classic acoustic event. The yellow arrows indicate the position where the classic acoustic event occurred above the intergranular lanes.

respectively. In addition, upward wave energy flux of up to $9.6 \times 10^6 \text{ erg s}^{-1} \text{ cm}^{-2}$ is found above the granule. The estimated wave energy flux is more than twice the value of $4 \times 10^6 \text{ erg s}^{-1} \text{ cm}^{-2}$ required for the chromospheric heating in a quiet Sun (Withbroe & Noyes 1977). The upward propagating waves eventually develop into shocks in the chromosphere. The shocks are identified as repetitive brightenings in the Ca II-0.5 Å images and $\lambda - t$ plot.

Our results suggest that the dynamic changes of granules can trigger transient waves above the granules. This is consistent with the mechanism of acoustic events associated with the darkening of intergranular lanes, which is considered a manifestation of downflows (Rimmele et al. 1995). Similarly, the dynamic changes of the granules can lead to downflows. According to simulation studies, the downflows can be induced by localized cooling events (Rast 1999) or by the deficiency of energy that supports the granule (Skartlien et al. 2000). The downflowing material rapidly descends below the surface of the photosphere, and when the material reaches a certain depth, it triggers vertical disturbances. Chae & Goode (2015) theoretically demonstrate that an impulsive disturbance in a gravitationally stratified medium produces acoustic waves of frequencies close to the cutoff frequency. The dominant period of the chromospheric oscillations we detected is about 3.8 min, which is slightly longer than the cutoff period of the internetwork region (~ 3 min). Nevertheless, according to Kayshap et al. (2018), successful propagation of photospheric 5 min oscillations to the chromosphere happens at some locations in the internetwork region of the quiet Sun, which might be the result of the magnetic field inclination. Our results also indicate that the formation of the Ca II brightenings are closely related to the 3 min band photospheric oscillations generated by the darkening granule event.

Is the new type of excitation event we observed physically distinct from the acoustic events reported in earlier studies? Our new-type events seem to show certain differences from the classic acoustic events. The classic acoustic events are found

predominantly in the intergranular lanes (Rimmele et al. 1995; Bello González et al. 2010; Malherbe et al. 2012). In our data, we also identified one classic acoustic event located in the intergranular lanes. Its physical properties and the time series are given in Section 3.3.4. However, our new-type events are not limited to the intergranular lanes. Rather, wave excitations initially occurred in the middle of the granules, where they began to collapse (see Figure 3.6), fragment (see Figure 3.7), or submerge (see Figure 3.8). Furthermore, the spatial extent of the excitation is much larger than that of the classic acoustic events.

Despite these differences, the new-type events do not seem to be physically distinct from the classic acoustic events. Darkenings and intense downflows characterize both types of events. In the case of the classic acoustic events, Rimmele et al. (1995) reported that intergranular lanes become darker several minutes before the excitation of waves. They suggested that the darkening reflects localized cooling that occurs in the intergranular lanes and that it is accompanied by downflows. Simulations by Skartlien et al. (2000) showed that the vanishing of small granules accompanies downflows and initiates acoustic waves. They noted that these collapsing granules are located at the boundaries of mesogranules, where the upward enthalpy flux is smaller than average. These collapsing granules may be the same type as the rapidly changing granules we observed. We are, therefore, the first to report the observational detection of the rapidly changing granules as the source of wave excitation predicted from the numerical experiment of Skartlien et al. (2000). We note that the same hydrodynamical process can account for both the acoustic events and the rapidly changing granules (Skartlien et al. 2000). Both types of events originate from the sudden cooling resulting from the deficit of upward convective energy flux. The cooling accounts for darkening, downflows, and the excitation of waves. In addition, we found that the classic acoustic event and the new-type acoustic events are similar in physical properties, such as the dominant period of the oscillations and the wave

energy flux. Since there is no physical difference, our events may be called acoustic events of a new type, and the previously reported events called classic acoustic events.

There is also the possibility that the two types of acoustic events may not form two distinct groups from the observational point of view. It is likely that some if not all photospheric darkening events or acoustic events reported in earlier studies (Rimmele et al. 1995; Cadavid et al. 2003) were in fact acoustic events of a new type. We find more dynamically changing granules in our data, and a follow-up study will explore their statical properties and relationship with the classic acoustic events.

Chapter 4

Temperature Variations in Internetwork Bright Grains

4.1 Introduction

Various dynamic phenomena such as intermittent brightenings (e.g., Martínez-Sykora et al. 2015), jets (e.g., Morton 2012) and fibrils that show up and down motions (e.g., De Pontieu et al. 2007; Skogsrud et al. 2016) prevail in the solar chromosphere. It is known that these dynamic phenomena are closely related to the wave propagation in the solar atmosphere. Generally, waves play a significant role in the transport of energy from the solar surface to the upper atmosphere. As the waves propagate upward, their amplitudes grow because of the density decrease with height. Shortly, they steepen into shock waves and the wave energy is converted into heat. The waves contribute to the heating of the chromosphere and corona. Therefore, to understand the processes of the energy transport and the heating in the solar atmosphere, it is necessary to study waves and the associated dynamic phenomena in the solar atmosphere.

In the internetwork region of the quiet Sun, small-scale ($1''$ – $2''$) roundish tran-

sient (~ 1 min) brightenings are observed ubiquitously. These brightenings are called internetwork bright grains or Ca II bright grains as they are commonly found in Ca II H and K images (for a review see Rutten & Uitenbroek 1991). These internetwork bright grains can be identified also in other chromospheric lines like Ca II 8542 Å and Mg II h and k lines (Cram et al. 1977; Vecchio et al. 2009; Martínez-Sykora et al. 2015). Recently, Martínez-Sykora et al. (2015) showed that the bright grains are conspicuous in the Mg II 2796 Å slit-jaw and Ca II 8542 Å line core images. As for their origin, it is widely accepted that they are produced by acoustic waves coming from the lower atmosphere. Kamio & Kurokawa (2006) suggested that Ca II H_{2V} grains are generated by 5 mHz oscillations in the photosphere below. Moreover, by using one-dimensional hydrodynamical simulation, Carlsson & Stein (1997) demonstrated that acoustic waves present in the photosphere propagate upward, and they develop into shocks in the middle chromosphere at heights of about 1 Mm. When the shocks are dissipated, the material in front of the shocks is compressed and heated appearing as bright grains in the chromosphere.

In this chapter, we report the detection of four internetwork bright grain events and the associated temperature enhancement in the chromosphere. Since the internetwork bright grains are caused by acoustic shocks formed in the middle chromosphere, a temperature enhancement is expected in these internetwork bright grains. We infer the hydrogen temperature at chromospheric level, and investigate its spatial and temporal relationship with the Ca II intensity and velocity. For this study, we analyzed high-spatial and high-spectral resolution data taken in the H α and Ca II 8542 Å lines obtained with the Fast Imaging Solar Spectrograph (FISS; Chae et al. 2013) installed on the 1.6 m Goode Solar Telescope (GST) at the Big Bear Solar Observatory (BBSO).

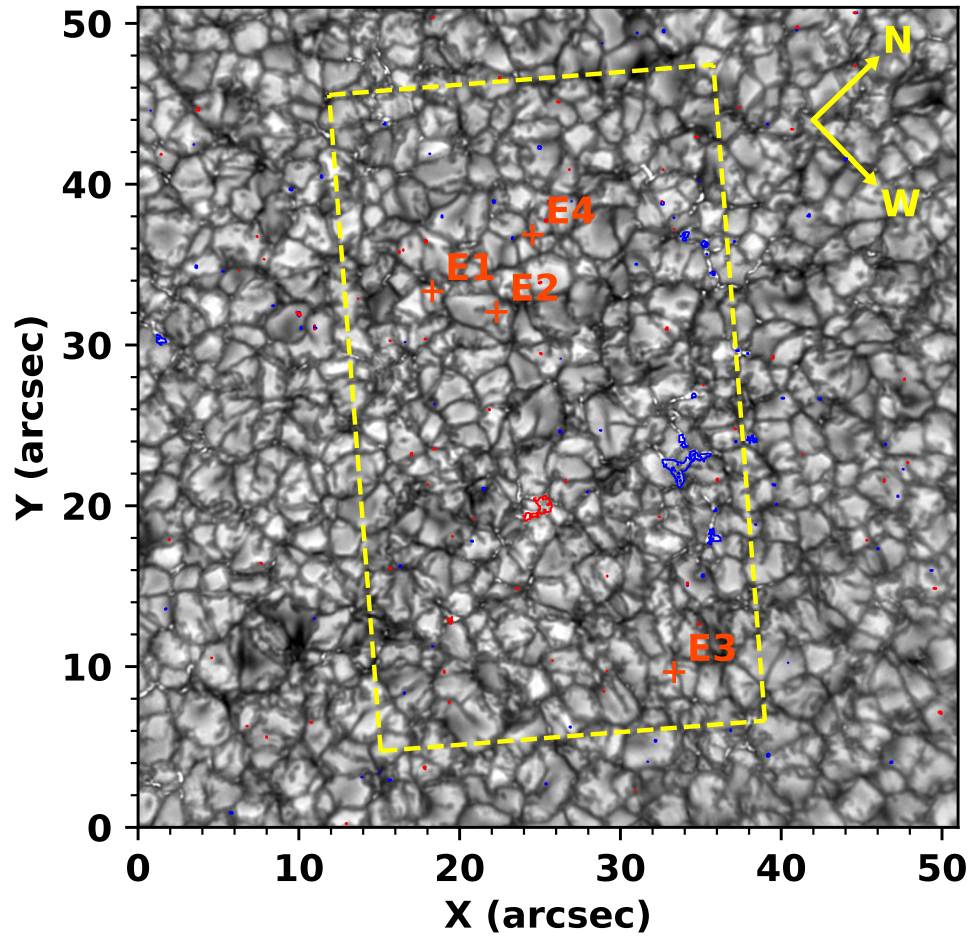


Figure 4.1 Photospheric TiO 7057 Å broadband filter image of a quiet-Sun region taken at 18:03:56 UT ($t = 11.9$ min). The dashed yellow line rectangle represents the FOV of the FISS. The locations of each event are marked with orange cross symbols and annotated as E1, E2, E3, and E4. The contours represent the line of sight (LOS) magnetogram obtained from the Near-Infrared Imaging Spectro-polarimeter (NIRIS) installed on the GST. The blue and red contours represent the LOS magnetic field strength of -100 G and 100 G, respectively.

4.2 Observations and data analysis

A quiet Sun region was observed on June 14, 2017 with the FISS. The region of our interest is located at heliocentric coordinates ($x = -140''$, $y = -70''$) and includes small part of internetwork and network regions (see Figure 4.1). The FISS records $H\alpha$ and $\text{Ca II } 8542 \text{ \AA}$ bands simultaneously by using two cameras. Raster images are acquired by fast scanning of a slit over the field of view (FOV). The slit is $0''.16$ wide and $40''$ long. The size of the FOV is $24'' \times 40''$, and the FOV was scanned every 27 s for an hour from 17:52:03 to 18:52:13 UT. The spatial sampling is $0''.16$, and the spectral sampling is 0.019 \AA in the $H\alpha$ line and 0.026 \AA in the Ca II line. The data processing was done as described in Chae et al. (2013), which includes the flat-field correction, distortion correction, and noise suppression.

We inferred the physical parameters of the chromospheric plasma using a multi-layer spectral inversion technique developed by Chae et al. (2020). Specifically, they employed a three-layer model of radiative transfer consisting of two chromospheric layers and one photospheric layer (see Figure 4.2). From the spectral inversion, 13 physical parameters can be determined. Among those parameters, we utilize line-of-sight (LOS) velocities at the photospheric (v_p) and upper chromospheric (v_1) layers, the source functions of Ca II line at various layers, and the Doppler widths of the upper chromosphere in the $H\alpha$ and Ca II lines. In particular, we can infer the temperature of the upper chromosphere by combining the values of the Doppler width in the $H\alpha$ and Ca II lines. The temperature is given in Chae et al. (2020) by the expression

$$T_H = 8100 \text{ K} \left[\frac{w_H}{0.025 \text{ nm}} \right]^2 \left(1 - 0.59 \left[\frac{w_{Ca}}{w_H} \right]^2 \right) \quad (4.1)$$

where w_H is the Doppler width of the $H\alpha$ line and w_{Ca} is the Doppler width of the $\text{Ca II } 8542 \text{ \AA}$ line.

To remove the granulation patterns corresponding to approximately 10 min or

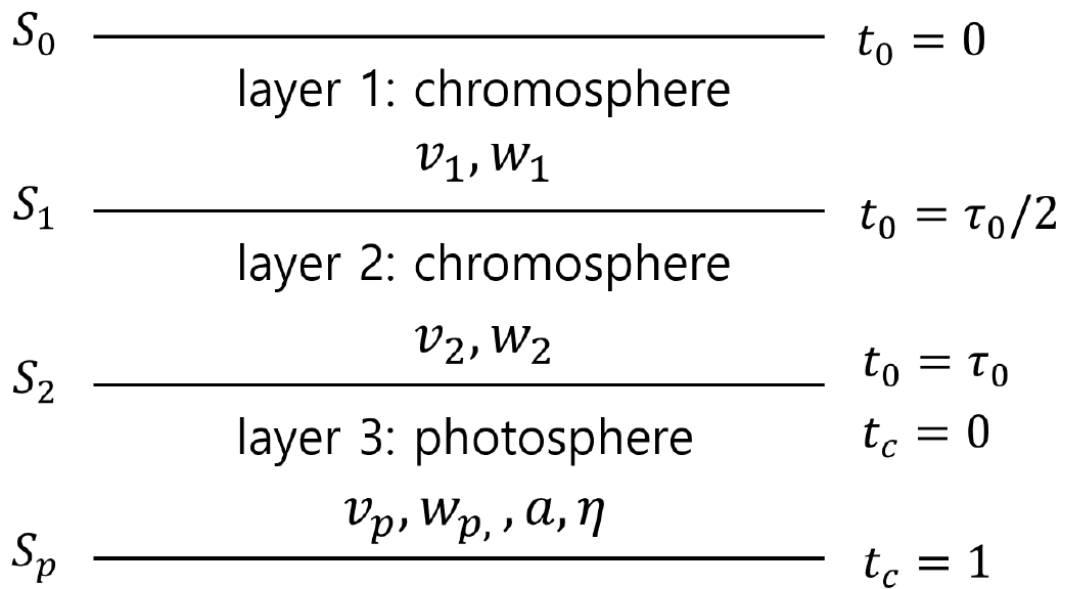


Figure 4.2 Three-layer model of radiative transfer consisting of two chromospheric layers and one photospheric layer (Chae et al. 2020).

even longer periodic fluctuations, we applied a bandpass filter of 1–6 min band to the photospheric and upper chromospheric velocities.

4.3 Results

We found four internetwork bright grain events in our data set. In previous studies, bright grains were mainly identified in the violet wings of Ca II H and K, i.e., Ca II H_{2V} and K_{2V} filtergrams, but they can be identified in the line core images of the Ca II 8542 Å line (Vecchio et al. 2009; Martínez-Sykora et al. 2015), and the blue wing images of the Ca II 8542 Å line as well (Kwak et al. 2020). In this study, we found three internetwork bright grain events in the Ca II 8542 Å line core images and one internetwork bright grain event in the Ca II-0.5 Å images.

Figure 4.3 presents the time series of the bright grains found in the Ca II line core images. The time zero ($t = 0$ min) is set to the moment of the first temperature peak. At $t = 0$ min, an elongated brightening can be identified in the center of the Ca II line core image (first row). It disappeared at $t = 2.2$ min. Even though several brightenings are present simultaneously, we only concentrate on the repetitive bright grains located in the center of the images. The bright grain recurred at $t = 4.4$ min and faded with time. The time interval between the brightenings is about 4.4 min and the size of the bright grain is about $2''$. The second row exhibits temporal evolution of the temperature in the chromosphere. Similar to the Ca II line core intensity, the temperature increased and decreased repetitively with almost identical period. Interestingly, the position of the bright grains are well aligned with those of the local temperature enhancement at $t = 0$ and $t = 4.4$ min. Likewise, all the internetwork bright grain events shown in Figure 4.4 to Figure 4.6 have spatial correspondence with the local temperature increase in the time series of the temperature maps.

Prior to the occurrence of the bright grains, photospheric darkening of the intergranular lanes is observed in all events in the Ca II-4 Å images (yellow arrow in

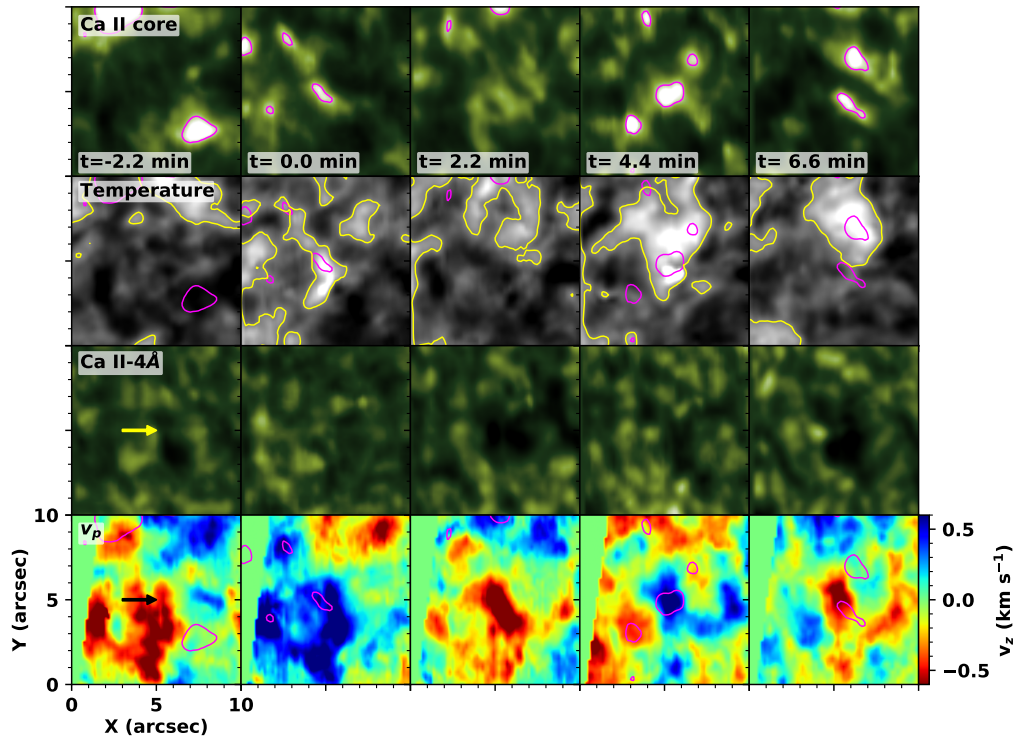


Figure 4.3 Time series of the $\text{Ca II}+0.0 \text{ \AA}$ raster images (first row), temperature maps (second row), the $\text{Ca II}-4 \text{ \AA}$ raster images (third row), and vertical velocity maps of the photosphere (fourth row) for event 1. The magenta contours on the $\text{Ca II}+0.0 \text{ \AA}$ raster images, temperature maps, and vertical velocity maps indicate the brightenings obtained from the $\text{Ca II}+0.0 \text{ \AA}$ images. The yellow contours on the temperature maps represent the area above 12 000 K. A yellow (black) arrow in the first $\text{Ca II}-4 \text{ \AA}$ image (vertical velocity map) marks the position where the repetitive internetwork bright grains occurred.

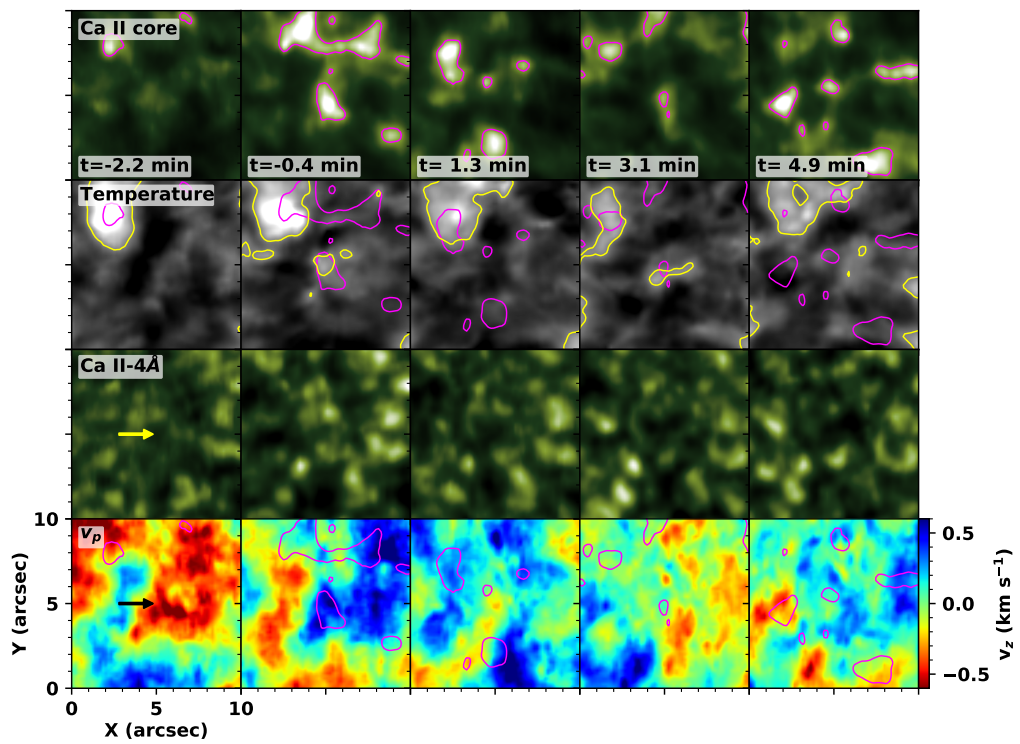


Figure 4.4 Same as Figure 4.3, but for event 2.

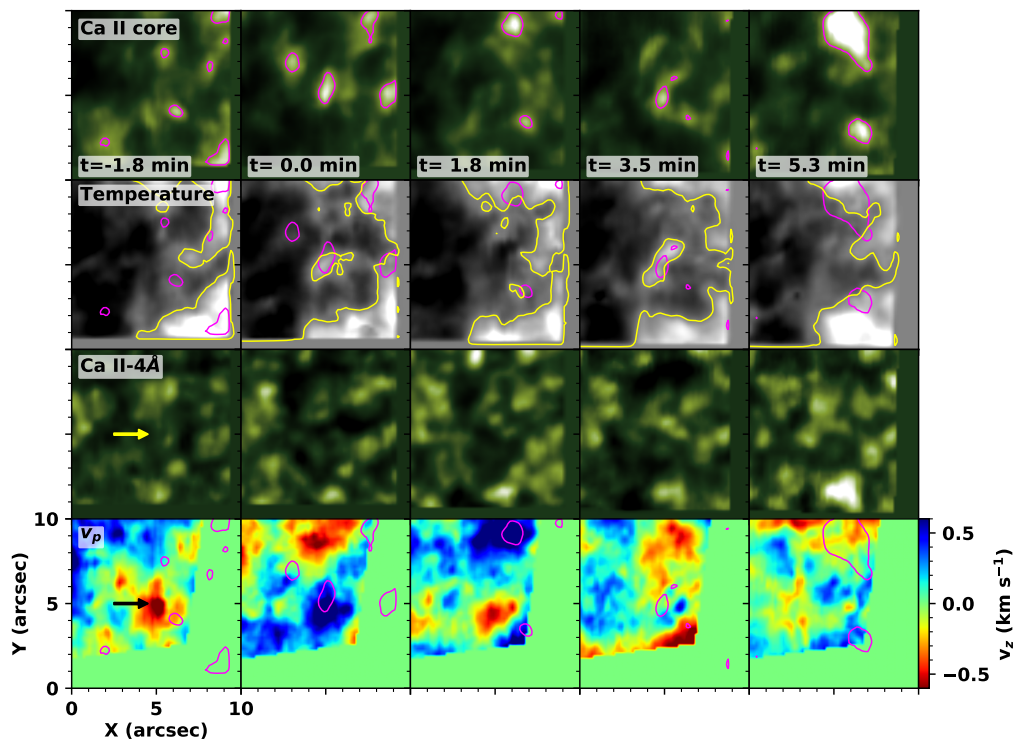


Figure 4.5 Same as Figure 4.3, but for event 3.

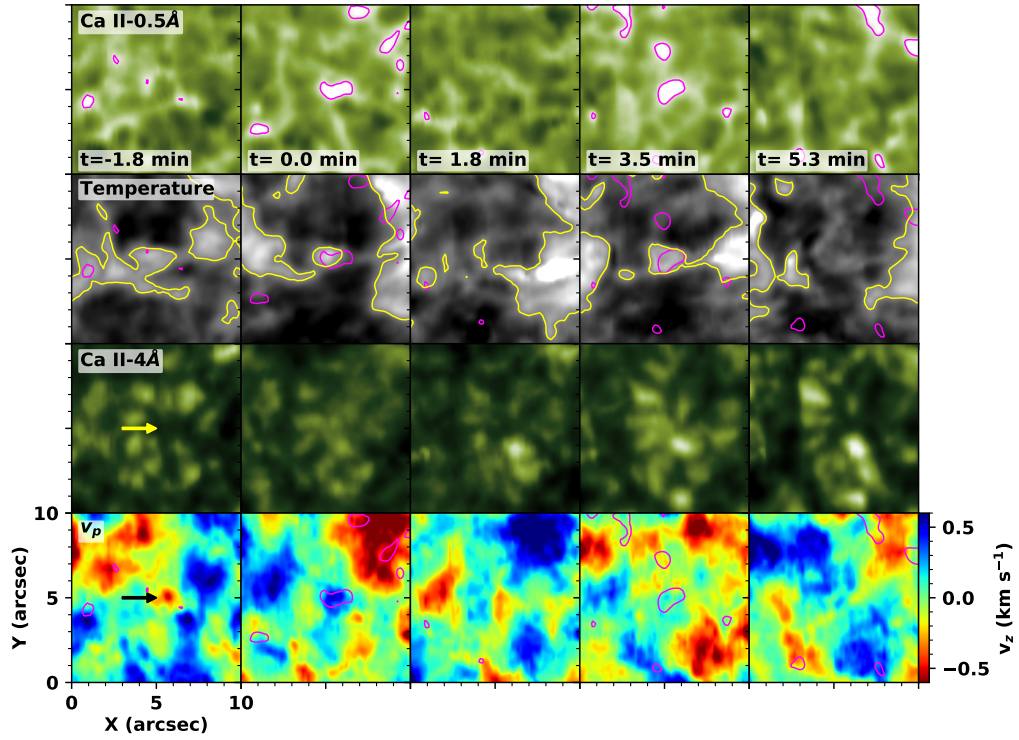


Figure 4.6 Time series of the Ca II-0.5 Å raster images (first row), temperature maps (second row), the Ca II-4 Å raster images (third row), and vertical velocity maps of the photosphere (fourth row) for event 4. The magenta contours on the Ca II-0.5 Å raster images, temperature maps, and vertical velocity maps indicate the brightenings obtained from the Ca II-0.5 Å images. The yellow contours on the temperature maps represent the area above 12 000 K. A yellow (black) arrow in the first Ca II-4 Å image (vertical velocity map) marks the position where the repetitive internetwork bright grains occurred.

Figure 4.3 to 4.6). In Figure 4.3, the intergranular lanes became dark at $t = -1.8$ min, but their brightness shortly recovered to normal at $t = 0$ min. This is consistent with previous studies of internetwork bright grains and their relation to a photospheric darkening (Cadavid et al. 2003; Kwak et al. 2020). The darkening is interpreted as convective downflows that occur in the intergranular lanes (Rimmele et al. 1995; Rast 1999; Kwak et al. 2020). In this region, the material raised by convection undergoes catastrophic cooling and falls down. Consequently, these convective downflows excite oscillations in the photosphere. In the vertical velocity maps of the photosphere, an oscillation pattern begins at $t = -2.2$ min. The downward and upward velocity patches appear alternately from $t = -2.2$ min to $t = 6.6$ min. These oscillations are well captured in the photospheric velocity maps since the dominant period of the oscillations is close to 4.4 min, which is the same as the time intervals of the bright grain reoccurrence.

Figure 4.6 shows the time series of a bright grain event found in the Ca II-0.5 Å images (first row). In comparison to the other three events, the bright grains of event 4 are not noticeable in the Ca II core images but they are conspicuous in the Ca II-0.5 Å images. Likewise, at $t = 0$ min, an elongated brightening appears in the center of the Ca II-0.5 Å image, but it disappears at $t = 1.8$ min. The bright grain recurred at $t = 3.5$ min and finally disappeared at $t = 5.3$ min. The time interval between the brightenings is about 3.5 min. The temporal evolution of the chromospheric temperature is presented in the second row. Similarly, the temporal evolution of the temperature follows the temporal variations of the Ca II-0.5 Å intensity. The bright grains are also colocated with the local temperature enhancement at $t = 0$ and $t = 3.5$ min.

Figures 4.7 to 4.9 present the temporal variations of the temperature, the intensity of the Ca II-0.5 Å and line core, the velocity of the upper chromosphere (v_1), and the source functions at two different chromospheric layers (S_0 and S_1) above

the bright grains in event 1, 2 and 3. In the case of event 1, which shows the largest temperature increase, the temperature variations include two peaks with the values of 16 700 K and 15 700 K at $t = 0$ min and $t = 4.4$ min, respectively. Before the bright grain event, the average temperature is about 9 700 K. The Ca II line core intensity peaks precede the temperature peaks by 27 s (corresponds to the cadence of our data), thus we can assume that they are very nearly co-temporal. The same pattern is found in the temporal variations of the source function S_0 . The temporal variations of S_0 is very similar to those of the core intensity. Indeed, the source function S_0 reflects the upper chromosphere very well, while the core intensity can be affected by the Doppler shifts in the upper chromosphere. Meanwhile, in the case of the Ca II-0.5 Å intensity and S_1 , the peaks relevant to the bright grains are not noticeable. The blueshift peaks of v_1 slightly lag the temperature peaks. This indicates that the temperature increases when the downward vertical velocity changes to upward, which is considered to be the shock front. In event 2 and 3, the temporal variations of each parameter show similar behavior with event 1.

In the same manner, Figure 4.10 shows the temporal variations of the parameters above the bright grains in event 4. The temperature variations include two peaks with the values of 13 800 K and 15 500 K at $t = 0$ min and $t = 3.9$ min, respectively. However, in comparison to the previous events, these temperature peaks are almost co-temporal with the intensity peaks of the Ca II-0.5 Å, not the intensity peaks of the line core. Similar to events 1, 2 and 3, the intensity peaks precede the temperature peaks by 27 s. The same pattern is found in the temporal variations of the source function S_1 . In contrast, in the case of the line core intensity and S_0 , the peaks relevant to the bright grains show very weak correlations. The line core intensities lag behind those of the Ca II-0.5 Å and S_0 , and it seems that the time difference reflects the height difference between the formation height of the Ca II-0.5 Å and line core. Other parameters look similar with those of events 1, 2 and 3.

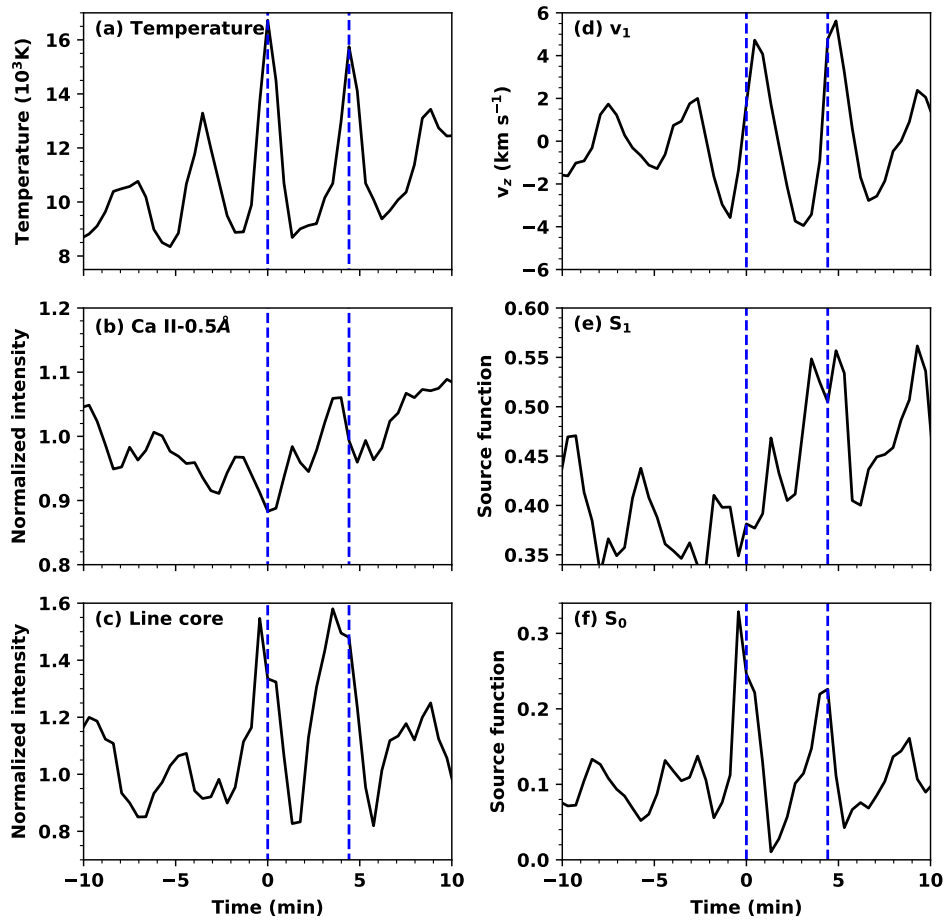


Figure 4.7 Temporal variations of temperature, intensity, vertical velocity and source functions at a fixed position of bright grains in event 1.

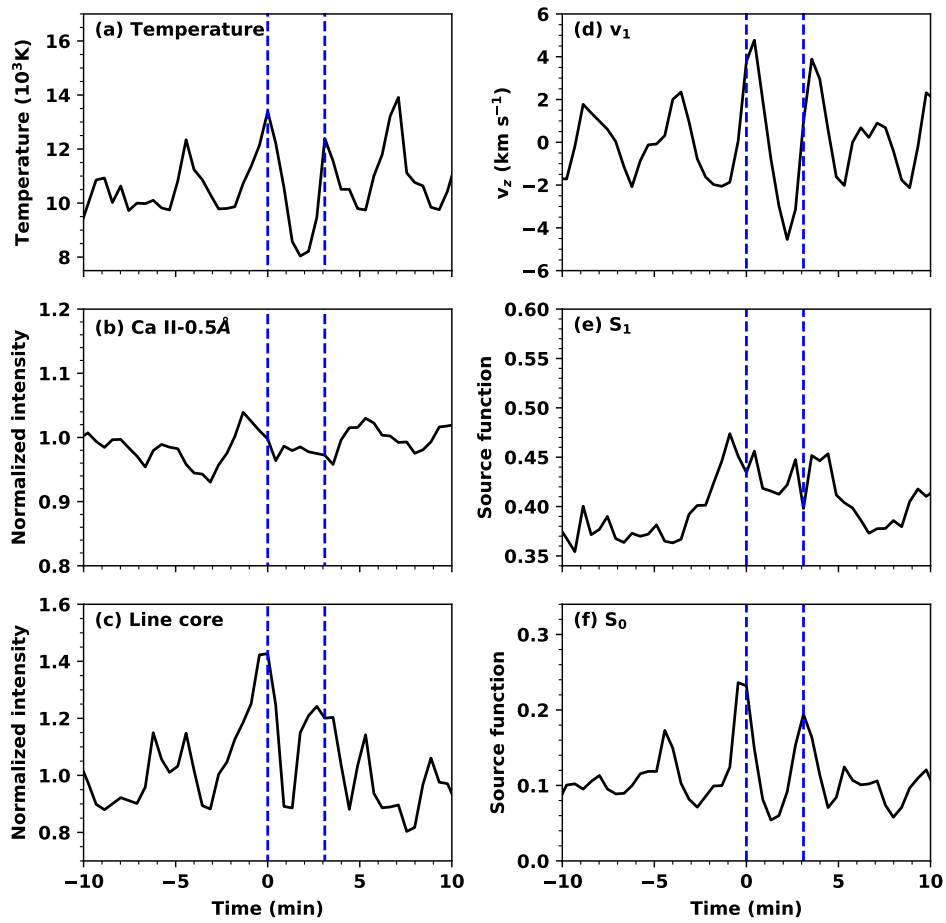


Figure 4.8 Same as Figure 4.7, but for event 2.

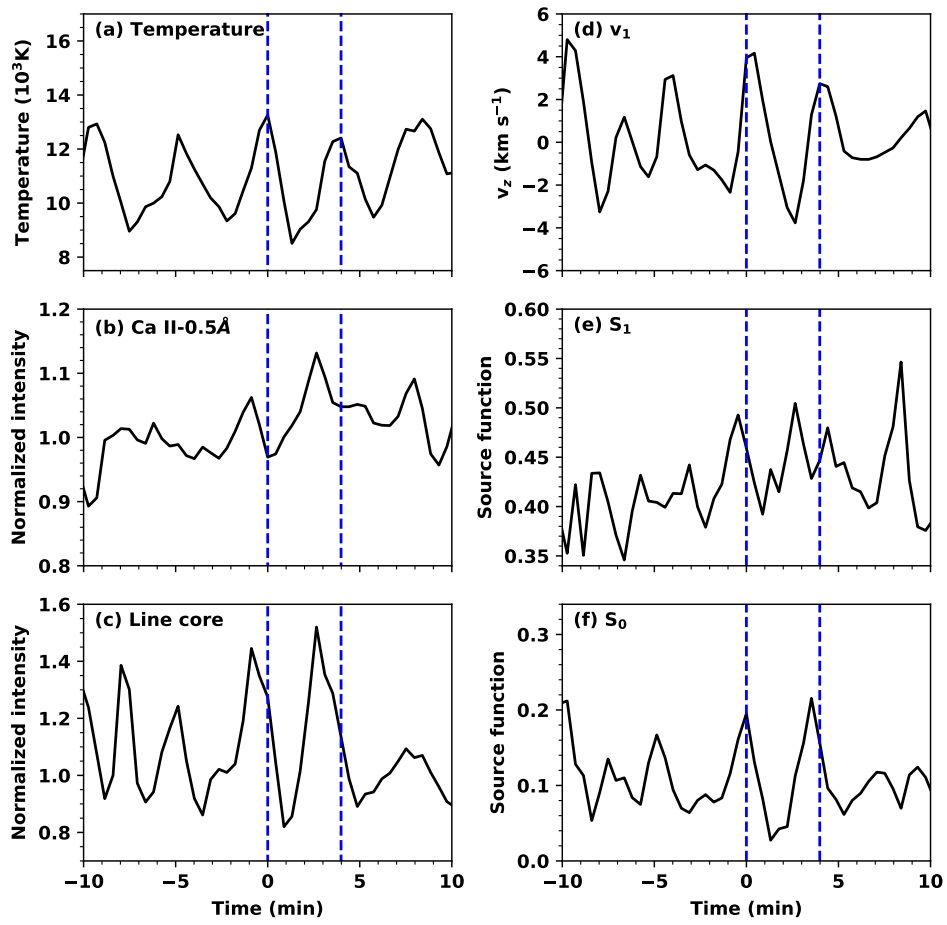


Figure 4.9 Same as Figure 4.7, but for event 3

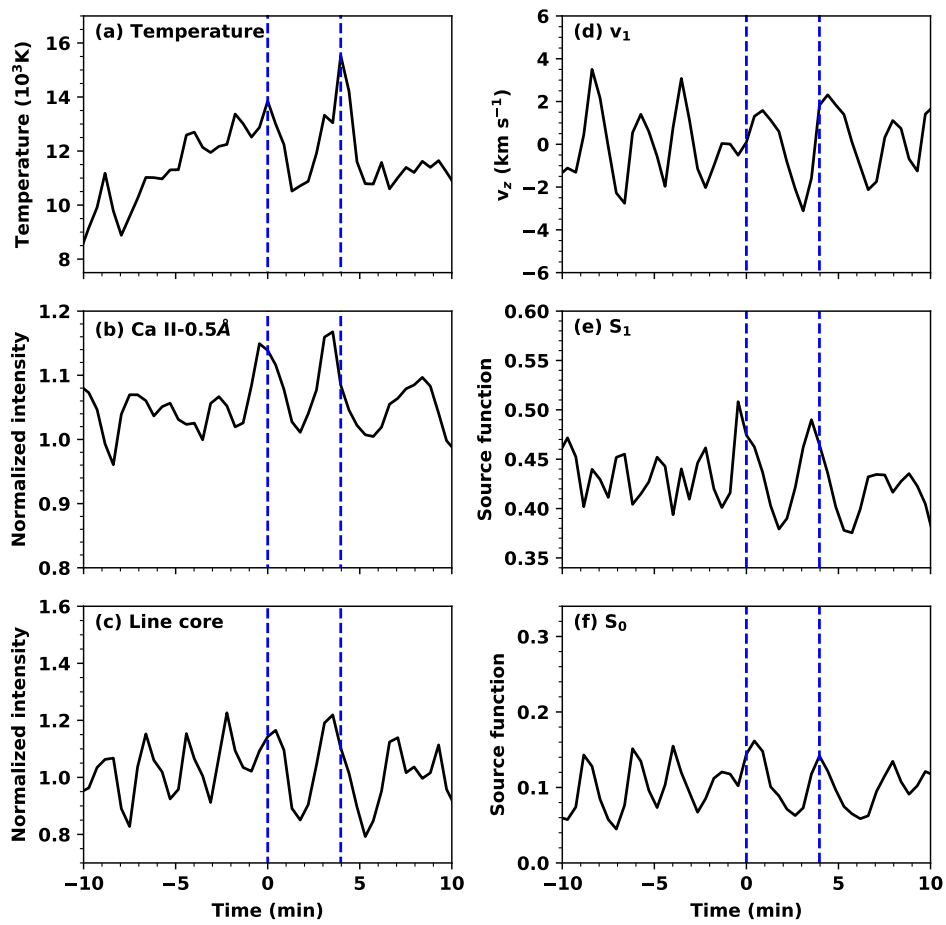


Figure 4.10 Same as Figure 4.7, but for event 4

The left panel of Figure 4.11 shows a wavelength-time ($\lambda-t$) plot of the Ca II 8542 Å line spectral profile at the center of the bright grains in event 1. Since this event shows the largest temperature increase among the four events we found, we chose this event for further analysis. In the $\lambda-t$ plot, a sawtooth pattern and the brightenings, which are regarded as manifestation of shocks, are prominent. The sawtooth pattern reflects the sudden appearance of a blueshifted feature that is followed by a slowly drift towards the redshifted feature. This pattern appeared twice after the first brightening occurred at $t = -0.4$ min with a period of about 3.9 min. The brightenings occurred when the Doppler shift changes from redshifted to blueshifted.

The brightenings have distinctive spectral line profiles. The top right panel of Figure 4.11 shows the Ca II spectral line profiles when the brightenings appear at $t = -0.4$ min (red) and $t = 3.5$ min (blue). The line profiles at the brightenings show enhanced core intensity compared to the reference profile (black). This is more obvious in the intensity contrast profiles. A contrast profile is defined as $C_\lambda = (I_\lambda - I_{ref})/I_{ref}$, where I_λ is the spectral intensity profile at one position, and I_{ref} is the reference profile obtained by temporally averaging the spectral intensity profiles at the same position. Strong emission is found in the wavelength ranges of -0.5 Å to 0.2 Å (see bottom panel of Figure 4.11). The emission is even stronger in the blue wing than the red wing. It implies that the plasma associated with the brightenings is placed at the formation height of the Ca II line core, and moves upward as the line profile reflects the mass motion of the plasma.

We identified the properties of the oscillations that produce the chromospheric bright grains in event 1. The velocity oscillations are detected in both, the photospheric and chromospheric layers. Figure 4.12 shows the temporal variations of the vertical velocities at the two atmospheric layers and the Ca II line core intensity. The dominant period of the oscillations that lead to the bright grains are 4.4 min in the photosphere and 4 min in the chromosphere. The amplitudes of the photospheric

and chromospheric velocities certainly increase in the time period from $t = -5$ min to $t = 10$ min. This stands out more clearly in the wavelet power spectra. In both the photosphere and chromosphere, the enhancement of the power is only confined to the time period from $t = -5$ min to $t = 10$ min. The calculated coherency between v_p and v_1 is above 0.93 within the period range of 3 min to 5 min. In addition, the phase differences between the v_p and v_1 is 0.6 rad, and it reflects the upward propagation of the waves from the photosphere to the chromosphere. Consequently, we confirmed that the internetwork bright grains are closely related to waves coming from the photosphere that have a dominant period of 4.4 min.

4.4 Discussion

In this chapter, we investigated the temperature variations in internetwork bright grains. We found four bright grain events in the Ca II 8542 Å raster images. Three of the four events are identified in the Ca II core images and one in the Ca II-0.5 Å images. In all events, when the bright grains are identified, corresponding temperature enhancements are found in the same location. Moreover, we examined the temporal variations of the line core intensity and temperature, and found a good correlation between them. In spite of the good temporal correlation, however, the peaks of the temperature lag behind those of the line core intensity by ~ 27 s (we remind that this is the data cadence). The dominant periods of the oscillations that cause the bright grains are 4.4 min and 4 min in the photosphere and chromosphere, respectively. Since the coherency between the photospheric and chromospheric velocities are high and the phase difference has positive values during the bright grain events, we conclude that the waves that cause the bright grains in the chromosphere come from the photosphere. The $\lambda - t$ plot of the Ca II line profile including the sawtooth pattern and the brightenings, reveal the existence of shocks in the chromosphere.

We found three bright grain events in the Ca II line core images and one bright

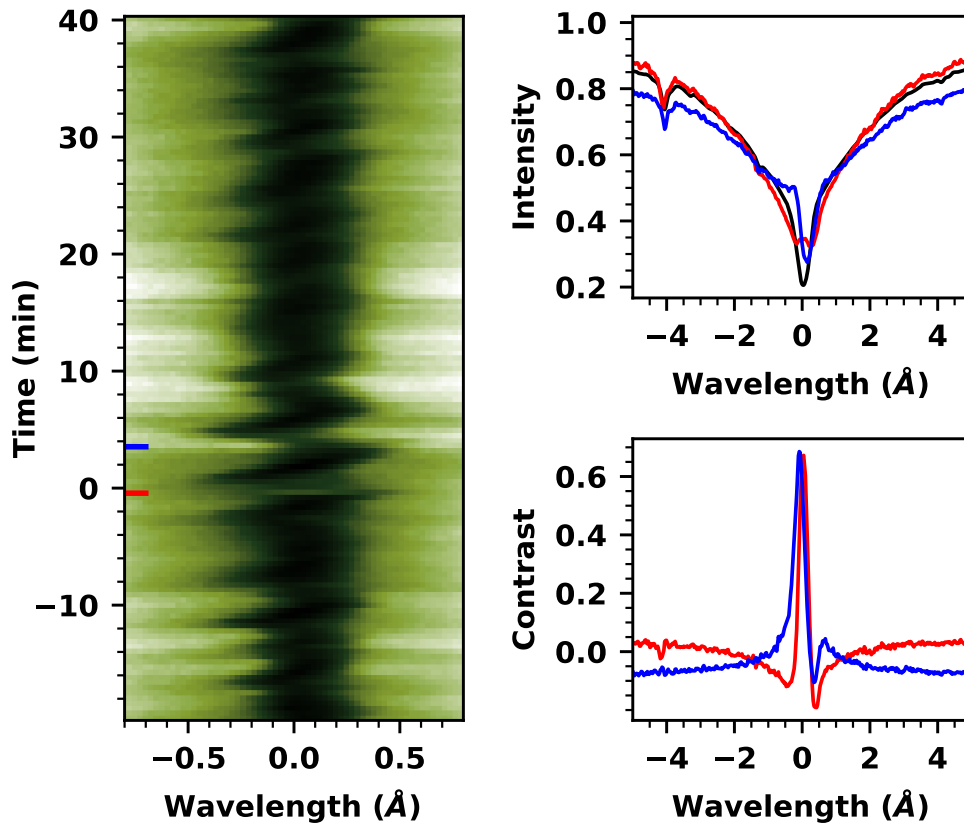


Figure 4.11 The wavelength-time plot ($\lambda - t$) of the Ca II 8542 Å line intensity (left), Ca II line profiles (top right), and contrast profiles (bottom right). The Ca II line profiles and contrast profiles are produced above internetwork bright grains in event 1 at $t = -0.3$ min (red) and $t = 2$ min (blue). The black solid line in the top right panel represents the average Ca II line profile produced from the same region.

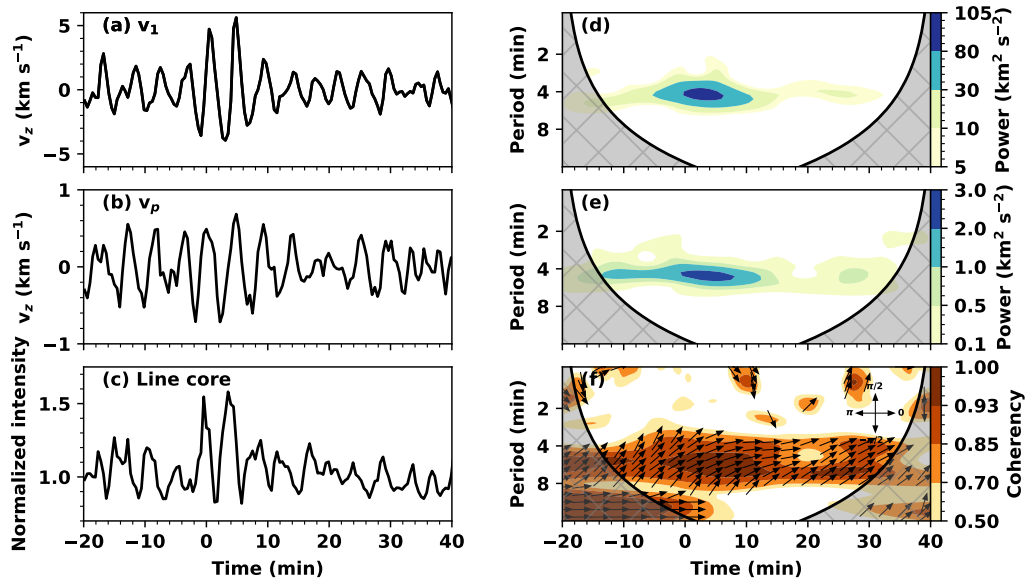


Figure 4.12 Left: Temporal variations of the chromospheric vertical velocity (a), photospheric vertical velocity (b), and Ca II line core intensity (c) in the center of the bright grains of event 1. Right: Wavelet power spectra of the chromospheric vertical velocity (d) and the photospheric vertical velocity (e). The coherence between the two time series of the velocity is shown by contours in (f). The phase differences at the points of coherence above 0.7 are denoted by the directions of the arrows.

grain event in the Ca II–0.5 Å raster images. One may wonder what is the difference between them. In Figure 4.7 to 4.10, we present the temporal variations of the intensities at the Ca II–0.5 Å and line core, and source functions at two different atmospheric heights. The source functions denoted by S_0 and S_1 are obtained from the multilayer spectral inversion (Chae et al. 2020), and correspond to the source functions at the upper boundary of the upper chromosphere, and the lower boundary of the upper chromosphere, respectively (see Figure 4.2). The bright grains in the event 1, 2 and 3 are noticeable in the temporal variations of the line core intensity and S_0 . In contrast, in case of event 4, the bright grains are prominent in the temporal variations of the Ca II–0.5 Å intensity and S_1 . It is well known that the occurrence of shocks in the chromosphere results in a larger source function (Carlsson & Stein 1997). Therefore, the response of the source functions at different atmospheric layers reflects the height of the shock formation. We suggest that the bright grains in event 4 are generated in the relatively lower atmosphere compared to those of event 1, 2, and 3.

We found a time difference of ~ 27 s between the Ca II intensity peaks and the temperature peaks during the internetwork bright grain events. We conjecture that the time difference resulted from the formation height difference of the Ca II and H α lines as the temperature actually represents the hydrogen temperature. The formation height of the Ca II 8542 Å line is about 1.3 Mm and that of the H α is about 1.5 Mm (Vernazza et al. 1981; Leenaarts et al. 2012). Therefore, the time difference of ~ 27 s can be explained by the propagation speed of the waves, which is considered to be close to the sound speed in the chromosphere.

Our results suggest that acoustic waves developing into shocks can increase the temperature in the upper chromosphere. It is well known that the energy carried by waves propagates upward and dissipates in the form of heat when the waves turn into shocks in the chromosphere. The enhancement of the temperature during the shocks

has been found in a simulation study of quiet Sun waves (Pietarila et al. 2006), but was never reported from observational analysis. In our study, we clearly showed that the temperature increases during the bright grain events, which are regarded as shocks produced in the chromosphere. The temperature begins to increase with the appearance of the shock front that is characterized by the sudden appearance of an upward motion changing into a downward motion.

In the internetwork region of the quiet Sun, a wealth of bright grains are observed that are considered as an observational signature of acoustic shocks. To what extent they can contribute to the chromospheric heating still remains an open problem. In a follow-up study, we will investigate the energy balance between the total wave energy that is supplied by waves characterized by bright grains and the total radiative loss at the same locations in the chromosphere.

Chapter 5

Summary and Conclusion

In this thesis, we investigated impulsive wave excitations observed in a sunspot umbra and internetwork region of the quiet Sun to understand the origin of acoustic waves in the solar atmosphere.

In Chapter 2, we investigated three-minute sunspot oscillations generated impulsively by a strong downflow event above a sunspot. We detected a strong downflow event and the associated oscillations in the same region by utilizing chromospheric lines (Ca II, H α , Mg II k 2796 Å) and transition region lines (C II 1336 Å, Si IV 1403 Å) obtained from the Fast Imaging Solar Spectrograph (FISS) and the Interface Region Imaging Spectrograph (IRIS). The downflows appear in the temporal variations of the Doppler velocity in the H α , C II, and Si IV lines, and subsequent oscillations are detected in all of the lines. The properties of the Doppler velocity oscillations are as follows. The amplitude of the oscillations is 2 km s⁻¹, and slightly decreases with time. The period of the oscillations gradually increases from 2.7 minutes to 3.3 minutes. These oscillation properties are consistent with those of the theoretical study of Chae & Goode (2015), which demonstrated the excitation of three-minute oscillations by impulsive disturbances in a gravitationally stratified medium. Our results suggest that three-minute oscillations can be triggered by a strong downflow

event that is regarded as a sunspot plume.

In Chapter 3, we investigated waves in the quiet Sun excited by granules that experience dynamic changes such as collapse (event 1), fragmentation (event 2), or submergence (event 3). The observations were carried out with the FISS and the TiO 7057 Å broadband filter imager. The granules become considerably darker than the surroundings when they undergo dynamic changes. According to previous studies, the darkening of the granules is interpreted as downflows occurring in the photospheric layer. After the dynamic changes of granules, which are involved with the downflows, oscillations are identified in the photospheric and chromospheric layers. In the case of oscillations detected in event 1, the dominant period of the oscillations is 4.2 min in the photosphere and 3.8 min in the chromosphere. We measured the wave energy flux of up to $9.6 \times 10^6 \text{ erg s}^{-1} \text{ cm}^{-2}$ above the granule. The estimated wave energy flux is larger than the value required for the chromospheric heating in a quiet Sun. These events may contribute to the heating of chromosphere. In the Ca II raster images, repetitive brightenings are found in the same location. These brightenings are regarded as the manifestation of shock waves. Our results suggest that dynamic changes of granules can produce acoustic waves that propagate upward and ultimately develop into shocks in the chromosphere.

In Chapter 4, we presented a study on the occurrence of internetwork bright grains and investigated their temperature variations in the upper chromosphere. The bright grains are small-scale transient brightenings occurring at three-minute intervals. They are regarded as the observational signature of shocks formed in the chromosphere. We acquired high-spatial and high-spectral resolution data taken with the FISS. We found four internetwork bright grain events in the Ca II 8542 Å raster images. Prior to the appearance of the bright grains in the chromosphere, intergranular lanes become dark in the photosphere, which is considered as convective downflows in the photosphere. We investigated the variations of the Ca II line inten-

sity and the temperature above the bright grains and found their spatio-temporal correlation. In event 1, we found a temperature increase of about 7 000 K. The temporal variations of the Ca II spectral line profiles reveal that the bright grains are produced by shocks as the bright grains occur between the maximum redshift and the maximum blueshift. Our results suggest that waves are excited by convective downflows in the photosphere, and these waves propagate upwards into the chromosphere. The waves develop into shock waves in the chromosphere and thus contribute to the increase of the temperature in the upper chromosphere as shocks dissipate.

Based on our results, the conclusion to be drawn here is that solar acoustic waves can be generated by impulsive events in the solar atmosphere. In this thesis, it has been shown that this occurs in a sunspot umbra and a internetwork region of the quiet Sun. Above a sunspot, a strong downflow event triggered 3 min oscillations, and in a quiet region, rapidly changing granules and convective downflows occurring in the intergranular lanes caused ~ 4 min period oscillations. These results are consistent with the theoretical study of Chae & Goode (2015) that demonstrated that waves with frequency corresponding to the acoustic cutoff arise as a natural response to impulsive disturbances. Furthermore, these waves propagate upward, carrying the wave energy into the upper atmosphere. As the waves steepen into shocks in the chromosphere, the energy carried by the waves dissipates into heat in the chromosphere.

Bibliography

- Aschwanden, M. J., Fletcher, L., Schrijver, C. J., & Alexander, D. 1999, *ApJ*, 520, 880
- Auchère, F., Froment, C., Bocchialini, K., et al. 2016, *ApJ*, 825, 110
- Bappu, M. K. V. & Sivaraman, K. R. 1971, *Sol. Phys.*, 17, 316
- Beckers, J. M., & Schultz, R. B. 1972, *Sol. Phys.*, 27, 61
- Beckers, J. M., & Tallant, P. E. 1969, *Sol. Phys.*, 7, 351
- Bello González, N., Franz, M., Martínez Pillet, V., et al. 2010, *ApJ*, 723, L134
- Bogdan, T. J., & Judge, P. G. 2006, *Philosophical Transactions of the Royal Society of London Series A*, 364, 313
- Brosius, J. W. 2005, *ApJ*, 622, 1216
- Brynildsen, N., Maltby, P., Foley, C. R., Fredvik, T., & Kjeldseth-Moe, O. 2004, *Sol. Phys.*, 221, 237
- Brynildsen, N., Maltby, P., Fredvik, T., Kjeldseth-Moe, O., & Wilhelm, K. 2001, *Sol. Phys.*, 198, 89
- Brynildsen, N., Leifsen, T., Kjeldseth-Moe, O., Maltby, P., & Wilhelm, K. 1999, *ApJ*, 511, L121

- Cadavid, A. C., Lawrence, J. K., Berger, T. E., et al. 2003, *ApJ*, 586, 1409
- Cao, W., Gorceix, N., Coulter, R., et al. 2010, *Proc. SPIE*, 7735, 77355V
- Carlsson, M. & Stein, R. F. 1997, *ApJ*, 481, 500
- Carlsson, M., & Stein, R. F. 2002, *ApJ*, 572, 626
- Centeno, R., Collados, M., & Trujillo Bueno, J. 2006, *ApJ*, 640, 1153.
- Chae, J., Park, H.-M., Ahn, K., et al. 2013, *Sol. Phys.*, 288, 1
- Chae, J., & Goode, P. R. 2015, *ApJ*, 808, 118
- Chae, J., Lee, J., Cho, K., et al. 2017, *ApJ*, 836, 18
- Chae, J., Madjarska, M. S., Kwak, H., et al. 2020, *A&A*, 640, A45.
- Cho, K., Chae, J., Lim, E.-. kyung ., et al. 2019, *ApJ*, 879, 67.
- Cram, L. E., Brown, D. R., & Beckers, J. M. 1977, *A&A*, 57, 211
- Cram, L. E. & Dame, L. 1983, *ApJ*, 272, 355
- De Pontieu, B., Title, A. M., Lemen, J. R., et al. 2014, *Sol. Phys.*, 289, 2733
- Deubner, F.-L. 1975, *A&A*, 44, 371
- Deubner, F.-L. & Fleck, B. 1990, *A&A*, 228, 506
- Deubner, F.-L., Waldschik, T., & Steffens, S. 1996, *A&A*, 307, 936
- De Pontieu, B., Hansteen, V. H., Rouppe van der Voort, L., et al. 2007, *ApJ*, 655, 624.
- Doyle, J. G., & Madjarska, M. S. 2003, *A&A*, 407, L29
- Fleck, B., & Schmitz, F. 1991, *A&A*, 250, 235

- Fontenla, J. M., Avrett, E. H., & Loeser, R. 1993, *ApJ*, 406, 319
- Giovanelli, R. G. 1972, *Sol. Phys.*, 27, 71
- Goldreich, P. & Kumar, P. 1990, *ApJ*, 363, 694
- Goode, P. R., Gough, D., & Kosovichev, A. G. 1992, *ApJ*, 387, 707
- Hoekzema, N. M., Rimmele, T. R., & Rutten, R. J. 2002, *A&A*, 390, 681
- Howard, R., Tanenbaum, A. S., & Wilcox, J. M. 1968, *Sol. Phys.*, 4, 286.
- Jefferies, S. M., McIntosh, S. W., Armstrong, J. D., et al. 2006, *ApJ*, 648, L151.
- Jess, D. B., Reznikova, V. E., Van Doorselaere, T., et al. 2013, *ApJ*, 779, 168.
- Kalkofen, W., Rossi, P., Bodo, G., & Massaglia, S. 1994, *A&A*, 284, 976
- Kamio, S. & Kurokawa, H. 2006, *A&A*, 450, 351
- Kayshap, P., Murawski, K., Srivastava, A. K., et al. 2018, *MNRAS*, 479, 5512
- Kayshap, P., Srivastava, A. K., Tiwari, S. K., et al. 2020, *A&A*, 634, A63
- Khomenko, E., & Collados, M. 2015, *Living Reviews in Solar Physics*, 12, 6
- Kobanov, N., Kolobov, D., Kustov, A., et al. 2013, *Sol. Phys.*, 284, 379.
- Kosovichev, A. G., & Zharkova, V. V. 1998, *Nature*, 393, 317
- Kosovichev, A. G. 2006, *Sol. Phys.*, 238, 1
- Kwak, H., Chae, J., Song, D., et al. 2016, *ApJ*, 821, L30.
- Kwak, H., Chae, J., Madjarska, M. S., et al. 2020, *A&A*, 642, A154.
- Lamb, H. 1909, *Proc. London Math. Soc.*, 7, 122

- Leenaarts, J., Carlsson, M., & Rouppe van der Voort, L. 2012, *ApJ*, 749, 136
- Lemen, J. R., Title, A. M., Akin, D. J., et al. 2012, *Sol. Phys.*, 275, 17
- Lites, B. W. & Thomas, J. H. 1985, *ApJ*, 294, 682.
- Lites, B. W. 1986, *ApJ*, 301, 992.
- Lites, B. W., Rutten, R. J., & Kalkofen, W. 1993, *ApJ*, 414, 345.
- Lites, B. W., Rutten, R. J., & Berger, T. E. 1999, *ApJ*, 517, 1013.
- Malherbe, J.-M., Roudier, T., Rieutord, M., et al. 2012, *Sol. Phys.*, 278, 241
- Malherbe, J.-M., Roudier, T., Frank, Z., et al. 2015, *Sol. Phys.*, 290, 321
- Maltby, P., Brynildsen, N., Fredvik, T., Kjeldseth-Moe, O., & Wilhelm, K. 1999, *Sol. Phys.*, 190, 437
- Martínez-Sykora, J., Rouppe van der Voort, L., Carlsson, M., et al. 2015, *ApJ*, 803, 44.
- Morton, R. J. 2012, *A&A*, 543, A6.
- Nagashima, K., Sekii, T., Kosovichev, A. G., et al. 2007, *PASJ*, 59, S631.
- Nakariakov, V. M., Ofman, L., Deluca, E. E., Roberts, B., & Davila, J. M. 1999, *Science*, 285, 862
- Nigam, R. & Kosovichev, A. G. 1999, *ApJ*, 514, L53
- Orrall, F. Q. 1966, *ApJ*, 143, 917
- O'Shea, E., Muglach, K., & Fleck, B. 2002, *A&A*, 387, 642
- Pietarila, A., Socas-Navarro, H., Bogdan, T., et al. 2006, *ApJ*, 640, 1142.

- Rast, M. P. 1999, *ApJ*, 524, 462
- Rimmele, T. R., Goode, P. R., Harold, E., et al. 1995, *ApJ*, 444, L119
- Roupe van der Voort, L. H. M., Rutten, R. J., Sütterlin, P., et al. 2003, *A&A*, 403, 277.
- Rutten, R. J. & Uitenbroek, H. 1991, *Sol. Phys.*, 134, 15
- Schrijver, C. J., Aschwanden, M. J., & Title, A. M. 2002, *Sol. Phys.*, 206, 69
- Shumko, S., Gorceix, N., Choi, S., et al. 2014, *Proc. SPIE*, 9148, 914835.
- Skartlien, R., Stein, R. F., & Nordlund, Å. 2000, *ApJ*, 541, 468
- Skogsrud, H., Roupe van der Voort, L., & De Pontieu, B. 2016, *ApJ*, 817, 124.
- Staude, J. 1999, in *ASP Conf. Ser. 184, Third Advances in Solar Physics Euroconference: Magnetic Fields and Oscillations*, ed. B. Schmieder, A. Hofmann, & J. Staude (San Francisco: ASP), 113
- Thomas, J. H., Lites, B. W., Gurman, J. B., & Ladd, E. F. 1987, *ApJ*, 312, 457
- Tian, H., DeLuca, E., Reeves, K. K., et al. 2014, *ApJ*, 786, 137
- Torrence, C., & Compo, G. P. 1998, *Bulletin of the American Meteorological Society*, 79, 61
- Ulrich, R. K. 1970, *ApJ*, 162, 993.
- Vecchio, A., Cauzzi, G., Reardon, K. P., et al. 2007, *A&A*, 461, L1.
- Vecchio, A., Cauzzi, G., & Reardon, K. P. 2009, *A&A*, 494, 269.
- Vernazza, J. E., Avrett, E. H., & Loeser, R. 1981, *ApJS*, 45, 635
- Withbroe, G. L. & Noyes, R. W. 1977, *ARA&A*, 15, 363

Wöger, F., von der Lühe, O., & Reardon, K. 2008, *A&A*, 488, 375

Zhao, J. & Chou, D.-Y. 2013, *Sol. Phys.*, 287, 149.

Zimovets, I. V., & Nakariakov, V. M. 2015, *A&A*, 577, A4

Zirin, H. & Stein, A. 1972, *ApJ*, 178, L85.

Zirin, H. 1974, *Sol. Phys.*, 38, 91

요 약

진동과 파동은 태양에서 흔하게 관측되는 현상이다. 파동은 통과해 지나온 매질에 대한 정보를 지니고 있으므로, 태양의 내부와 대기 등, 태양을 전반적으로 탐구하기 위해서는 태양에서 관측되는 파동 현상에 대한 이해와 심도 있는 연구가 필요하다. 파동은 태양 대기에서의 온도, 밀도, 자기장 구조 등에 의존하며, 태양 대기에서 발생하는 다양한 물리적 현상들과도 관련이 있다. 따라서 파동은 태양의 대기 구조와 그곳에서 발생하는 다양한 물리적 과정을 연구하는데 매우 유용한 진단 도구이다. 또한 파동은 태양의 내부와 표면에 존재하는 에너지를 상층 대기로 전달하여 채층과 코로나 가열에 기여한다. 지금까지 파동에 대해 많은 연구가 이루어져 왔지만 그 기원에 대해서는 아직 완전히 밝혀지지 않았다. 파동 발생에 대한 연구는 주로 이론적인 관점에서 이루어져 왔으며, 관측적으로도 활발히 연구되어야 할 필요성이 있다. 본 학위 논문에서는 태양 대기에서의 충동적 교란(impulsive disturbance)에 의해 음파가 발생하는 현상에 대해 연구한다. 본 연구를 위해 빅베어 태양 천문대(Big Bear Solar Observatory, BBSO)의 1.6미터 태양 망원경(Goode Solar Telescope, GST)에 설치되어 있는 고속영상 태양분광기(Fast Imaging Solar Spectrograph, FISS)와 소규모 관측 위성인 인터페이스 영역 영상분광기(Interface Region Imaging Spectrograph, IRIS)를 사용하여 고분해능의 자료를 획득하였다.

먼저, 태양 흑점 위에서 강한 하강 물질(strong downflow)에 의해 충동적으로 생성된 3분 진동에 대한 연구를 수행하였다. 이 진동은 흑점 암부에서 관측되는 지속적인 3분 진동과는 다르게 일시적으로 발생한다. 본 연구에 활용한 자료는 1.6 미터 태양 망원경(GST)에 설치되어 있는 고속영상 태양분광기(FISS)와 인터페이스 영역 영상분광기(IRIS)를 사용하여 획득하였다. 흑점 암부에서 발견되는 강한 하강 물질 사건(strong downflow event)은 채층 분광선과 천이영역 분광선에서 확인되었으며, 그 이후 같은 지역에서 진동이 발생하는 것도 확인하였다. 도플러 속도 진동의 특성들도 조사하였다. 진동의 진폭은 2 km s^{-1} 이며, 시간에 따라 점차 감소한다. 진동의 주기는 초기에는 2.7분이나 점차 증가하여 3.3분에 이르게 된다. 강한 하강 물질의 특성은 흑점 플룸(sunspot

plume)의 특성과 잘 일치한다. 우리의 결과를 바탕으로, 3분 진동은 중력 층화된 대기에서 하강 층동 사건(impulsive downflow event)에 의해 발생하는 것을 확인하였으며, 이는 Chae & Goode (2015)의 이론적 연구 결과와 잘 일치한다.

둘째로, 정온지역에서 빠르게 변화하는 쌀알무늬(granule)에 의해 생성되는 파동에 대한 연구를 수행하였다. 분석에 사용한 자료는 고속영상 태양분광기(FISS)와 광대역 필터 영상기(Broadband Filter Imager, BFI)를 활용하여 획득하였다. 획득한 관측 자료에서는 붕괴되거나(collapse) 분열하거나(fragmentation) 침강하는(submergence) 쌀알무늬가 발견되었다. 쌀알무늬에서 이러한 급격한 변화가 일어날 때, 쌀알무늬의 밝기는 그 주변 지역의 쌀알무늬들보다 매우 어두워진다. 쌀알무늬의 이러한 급격한 변화 이후 광구와 채층에서는 일시적인 진동이 발생한다. 붕괴되는 쌀알무늬의 경우, 이때 발생한 진동의 주기는 광구에서 4.2분이고 채층에서 3.8분이다. 같은 위치의 Ca II 채층 이미지에서는 반복적으로 밝아지는 현상(intermittent brightening)이 발견되었는데, 이는 충격파 현상에 의한 것으로 알려져 있다. 우리의 결과를 바탕으로, 정온지역에서 쌀알무늬의 역동적인 변화가 파동을 생성하며, 이 파동이 상층 대기로 전파하여 채층에 도달하면 궁극적으로는 충격파로 발전될 수 있다는 것을 시사한다.

셋째로, 우리는 정온지역 밝은 알갱이(internetwork bright grain)의 발생과 이와 관련된 채층 상층부의 온도 변화에 대한 연구를 수행하였다. 밝은 알갱이는 Ca II 이미지에서 관측되는 작은 규모의 반복적인 밝기 강화(small-scale intermittent brightening) 현상인데, 이는 채층에 형성된 충격파에 의한 것으로 알려져 있다. 우리는 고속영상 태양분광기를 사용하여 고해상도 분광 자료를 획득하였고, Ca II 이미지에서 정온지역 밝은 알갱이 사건(internetwork bright grain event)을 네 건 발견하였다. 우리는 밝은 알갱이에서 Ca II 강도(intensity)와 온도 변화를 조사하였고, 그들의 변화 양상이 시공간적으로 서로 잘 일치하는 것을 확인하였다. 채층에서 밝은 알갱이가 나타나기 이전에 광구 이미지에서는 쌀알무늬의 사이의 공간(intergranular lanes)이 어두워지는데, 이는 대류에 의해 상승했던 물질이 하강하는 현상으로 여겨진다. 가장 강한 온도 상승을 보였던 첫번째 사건을 자세히 조사하였다. 밝은 알갱이가 발생할 때 온도는 약 7000 K 가량 상승하는 것을 확인하였다. Ca II 스펙트럼선의 시간에 따른 변화는 밝은 알갱

이가 충격파에 의해 생성된다는 것을 보여준다. 이는 밝아지는 현상이 최대 적색편이 (redshift)와 최대 청색편이(blueshift) 사이에 발생하기 때문이다. 우리의 결과를 바탕으로, 광구에서의 파동은 대류에 의해 상승했던 물질이 하강하면서 발생하게 되며, 이 파동이 채층으로 전파되면서 충격파로 발전하게 되고 결국 소멸되면서 채층 상층부의 온도를 상승시킨다는 것을 확인하였다.

본 학위 논문의 세부 주제들은 태양 대기에서 발생한 충동적 사건들에 의해 음파가 생성될 수 있음을 시사한다. 이때 발생한 파동은 위로 전파되어 상층 대기인 채층과 코로나에 도달하며, 파동에 의해 운반되는 에너지는 상층 대기에서 열로 전환되어 채층과 코로나 가열에 기여한다.

주요어: 태양: 대기 - 태양: 광구 - 태양: 채층 - 태양: 진동 - 태양: 흑점 - 방법: 관측

학 번: 2012-20397